University of Warsaw
Faculty of Physics

Maciej Giza

Record book number: 382610

Study of the $\Lambda_b^0 \rightarrow D_s^- p$ decays at the LHCb experiment

Master's thesis
in the field of Physics

The thesis was written under the supervision of:

Agnieszka Dziurda, BEng, PhD
Polish Academy of Sciences
The Henryk Niewodniczański Institute of Nuclear Physics (PAN)

Jacek Ciborowski, PhD, DSc, ProfTit
Particles and Fundamental Interactions Division
Institute of Experimental Physics

Warsaw, June 2021

Summary

In this Master's thesis, the operation principles of LHC accelerator and LHCb detector are referred to. They are followed by the properties description of the LHCb tracking and particle identification systems. One of the beauty to charm flavour decays, $\Lambda_b^0 \to D_s^- p$, has never been observed. Its branching fraction is proportional to the CKM matrix element V_{ub}, which precise determination is a crucial test of the CKM unitarity. To minimise any systematic effects, this branching fraction can be measured with respect to the $\overline{\Lambda}_b^0 \to \overline{\Lambda}_c^- \pi^+$ normalisation channel. The main goal of this thesis focuses on the data-driven approach used for the efficient estimation of background contributions in the $\Lambda_b^0 \to D_s^- p$ sample. Two statistically independent control samples of the $B_s^0 \to D_s^- \pi^+$ and $B_s^0 \to D_s^\mp K^\pm$ decays are employed. Together with the signal ($\Lambda_b^0 \to D_s^- p$) and normalisation ($\overline{\Lambda}_b^0 \to \overline{\Lambda}_c^- \pi^+$) modes they are used for the unbiased yields determination. For each channel, the beauty hadron invariant mass distribution is fitted taking into account many possible background contributions. The procedure results in the determination of (102 ± 14) and (835 ± 35) $\Lambda_b^0 \to D_s^- p$ candidates for LHC Run1 (2011-2012) and Run2 (2015-2018) data taking periods, respectively. In addition, a high statistic normalisation mode $\overline{\Lambda}_b^0 \to \overline{\Lambda}_c^- \pi^+$ is examined, finding (64050 ± 260) and (367820 ± 660) candidates in Run1 and Run2 data samples. Provided in this dissertation studies about these decays are part of the ongoing LHCb measurement performed in the collaboration with NIKHEF group from the Netherlands.

Keywords

particle physics, LHC, branching fraction, flavour physics

Title of the thesis in Polish language

Badanie rozpadu $\Lambda_b^0 \to D_s^- p$ w eksperymencie LHCb

Acknowledgements

Throughout writing this thesis, I have received lots of support and assistance.

First and foremost, I would like to thank my supervisor, Dr Agnieszka Dziurda, who has shown trust, exceptional patience, encouragement and support towards me. Your insightful feedback brought my work to a higher level. Thank you for being able to make time for regular meetings and eagerly answering any kinds of questions that arose.

I want to thank Prof. Jacek Ciborowski as the second supervisor to this thesis for his examination of my thesis work.

I am very grateful for the Lb2DsP group, including Prof. Tomasz Szumlak, Dr Niels Tuning, Dr Sevda Esen and Jordy Butter for the great working environment, positive atmosphere and constructive discussions over the months that have brought plenty of benefits for this thesis.

I would like to specially thank Prof. Aleksander Filip Żarnecki and other University of Warsaw Faculty of Physics authorities for trusting me with the choice of my work's topic and the harmonious cooperation. The thesis would not be possible without your help.

Last, but definitely not least, I would like to thank my family and friends, who gave me the continuous support throughout the year. In times of Covid-19 pandemic, your love has never been more precious.

Papers should be correct,
talks should be interesting,
and theses should be handed in.

Burton Richter
(codiscoverer of J/ψ meson in 1974)

Contents

Chapter 1

Introduction

Ever since the very early civilizations took their first steps, humans aspired to understand the world which surrounded them. On top of the close environment, other two frontiers have brought our ancestors attention: the infinitely small and the infinitely large. An overabundance of new experimental and theoretical results over the past decades has drawn a picture of vast micro- and macrocosm, closely related to each other. The scientific research have often been found to be a foundation of technical progress and thus source of well-being improvement for all people. Attempts to find answers to the fundamental questions are necessary to understand the environment, the origins and the conditions for existence of humankind, constituting part of cultural heritage.

One of the questions, that troubled people for more over 2000 years, is the nature of matter. Greek philosophers argued whether the substance of which the living creatures, planets and the stars are made comprise the indestructible atoms, like Democritus stated, or the regular bodies and four elements, as Plato thought. It might seem that the scientific development found arguments in favour of both possibilities [1].

Newton's proposal of constituents of matter was to treat it as composed of infinitely hard smooth balls [2] and to introduce gravity as the force of interaction. The idea of indivisible building blocks kept together by certain forces held strong over the past 200 years. Only the nature of these blocks and forces has been changing: from the elements discovered by the chemists, found divisible to the form of nucleus surrounded by an electron cloud, to the atomic nuclei build out of protons and neutrons. In 1931 the positron was discovered by Carl D. Anderson [3] and the idea the neutrino existence was propagating in the scientific community as Wolfgang Pauli wrote an open letter to the nuclear physicists in December the previous year [4]. These historical events distorted the simple image of all matter composed of only three types of particles, suggested presence of antimatter and a new force, the weak interaction. Finally, the numerous particles detected over the years could be understood by means of quarks and antiquarks, interacting by the strong nuclear force, well described by the quantum chromodynamics QCD with the presence of gluons, the force carriers, that are accompanied by three families of leptons, all considered to be fundamental [1].

One might ask whether quarks and leptons truly are indivisible particles or if they possess a structure within, an issue previously considered by the philosopher Immanuel Kant [5]. If the building blocks have spatial extension, why could not they be divided into smaller parts? Alternatively, the building blocks are mathematical points, but then it is non-trivial how they can have a mass, charge and spin.

One of the most intriguing signs of progress in physics is the change of paradigms. Indeed, the concept of ultimate building blocks must fail in presence of quantum interactions. For quarks, it is impossible to break them apart, as their binding energy becomes so strong that any energy applied to separate them creates new quark-antiquark pairs. The fact that antimatter exists implies that matter is not 'eternal', it can annihilate and in reverse, be produced from energy in form of particle-antiparticle pairs. All those experimental observations contributed to the recognition that the symmetry principles are at the basis of our comprehension of nature, in such stark contrast to the idea of building blocks and acting forces. 'Nature does not know' how we observe it, thus it seems logical that the laws of physics should be invariant under certain transformations, e.g. choices of the origin of the coordinate system, its orientation in space and the moment of starting the measurement are arbitrary, so the laws deduced from such observations should not depend on them [1]. It has been proposed by Emmy Noether that the invariance of laws of physics under certain continuous transformation results in conservation of a physical property [6]. Great examples are translations and rotations in space and time which result in that correspondingly momentum, angular momentum and energy are constant. However, not only the continuous symmetries are the subject of the Noether's theorem, but also the discrete ones. The mirror transitions, like spatial reflection P, particle-antiparticle exchange C and time reversal T, manifested themselves as the conservation of parity, charge conjugation and balance rules in reactions, all necessary for proper calculations in quantum mechanics.

The parity violation in weak interactions, discovered in 1957 for β decay of cobalt isotop Co^{60} in C. S. Wu experiment [7], as proposed by T. D. Lee and C. N. Yang [8], remained a puzzle for the physicists. In the following years, experiments have shown that the C conservation is completely violated, the combined CP symmetry is violated, almost unnoticeably and CPT symmetry is considered to be invariant as for this day.

For the quantum field theories, the most intriguing class of transformations are the gauge symmetries. In case of electrodynamics, fields given by the Maxwell's equations are determined by the condition that gauge symmetry takes place, thus making them independent against potentials' gauge transformations. By analogy, the strong and weak interactions are also described by gauge symmetries, in which case the breaking of the symmetries is an important issue.

Thus, thanks to the progress in particle physics, in both theory and experiments, the description of nature with the abstract terms of symmetries and their breaking took over the models of hard indestructible spheres - moving away from Democritus to Plato. The peak achievement of scientific development emerged in the form of the "Standard Model of Particle Physics" (SM), shown to be a renormalisable gauge theory, encapsulating all known particles and interactions between them in the comprehensible manner. The SM is visualised in Fig. 1.1 listing three generations of fermions (quarks and leptons) which constitute matter and five bosons as the force carriers (W and Z bosons for the weak force, photons γ for the electromagnetic force, gluons g for the strong force).

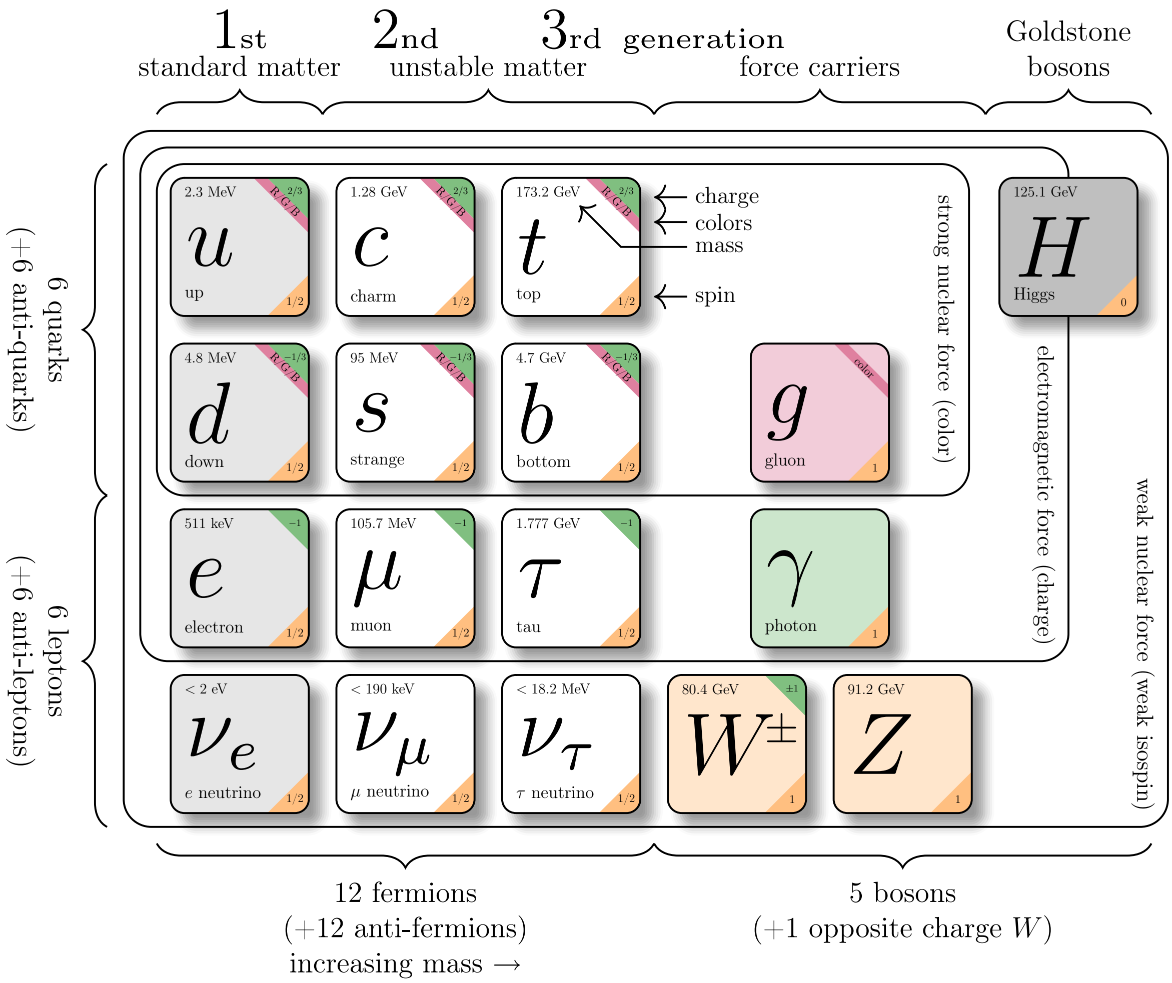

Figure 1.1: A Standard Model visualisation with distinction between quarks, leptons, force carriers and the Goldstone boson (Higgs boson). The particles are affected by the force blocks they are in. The picture taken from the table made by David Galbraith and Carsten Burgard at the CERN Webfest 2012 [9].

Three forces exist in the Standard Model: the strong force, the electromagnetic force and the weak force. The latter is the weakest of them all and as the only one it allows for a quark to change its flavour to another generation. The first attempt to describe the coupling of the weak interaction in a matrix, for the two generations known at the moment, was made by N.Cabibbo [10]. Later on, M.Kobayashi and T.Maskawa rewrote this matrix to the form shown in Eq. (1.1), which is currently known as the Cabbibo-Kobayashi-Maskawa (CKM) matrix V_{CKM} [11] and reflects the fact that the flavour eigenstates (d', s', b') do not coincide with the mass eigenstates (d, s, b):

$$\begin{pmatrix} d' \\ s' \\ b' \end{pmatrix} = V_{CKM} \begin{pmatrix} d \\ s \\ b \end{pmatrix} = \begin{pmatrix} V_{ud} & V_{us} & V_{ub} \\ V_{cd} & V_{cs} & V_{cb} \\ V_{td} & V_{ts} & V_{tb} \end{pmatrix} \begin{pmatrix} d \\ s \\ b \end{pmatrix}. \tag{1.1}$$

The matrix elements V_{ij} correspond to the flavour-changing weak coupling between the respective quarks q_i and q_j. The CKM matrix is required to be unitary from the fact that it describes the transformation between the orthogonal bases of the weak force eigenstates and the quark mass (physical) states [12].

According to the Sakharov's conditions for the baryon-antibaryon asymmetry that is observed today [13,14], the CP breaking should be measured at much higher level than it is predicted by the Standard Model, so that more matter than antimatter could be created in ongoing processes. In order to check what is the reason for that difference, the consistency of the CKM framework has been tested. The CKM parameters are measured with higher precision to test the unitarity of the matrix they compose.

The unitarity relations throw light on the unitarity property of the CKM matrix. One of these relations is:

$$V_{ub}^{*}V_{ud} + V_{cb}^{*}V_{cd} + V_{tb}^{*}V_{td} = 0. \tag{1.2}$$

When divided by $V_{cb}^{*}V_{cd}$, relation in Eq. (1.2) can be visualised as a unitary triangle in the complex plane. The CKMFitter group [15] combined the measurements on parameters from this equation into the unitarity triangle as shown in Fig. 1.2. The dark green band corresponds to the CKM matrix element V_{ub} magnitude. It is one of the least known CKM element due to its large uncertainty. Further research towards establishing more precise value of $|V_{ub}|$ thus constitute an interesting issue.

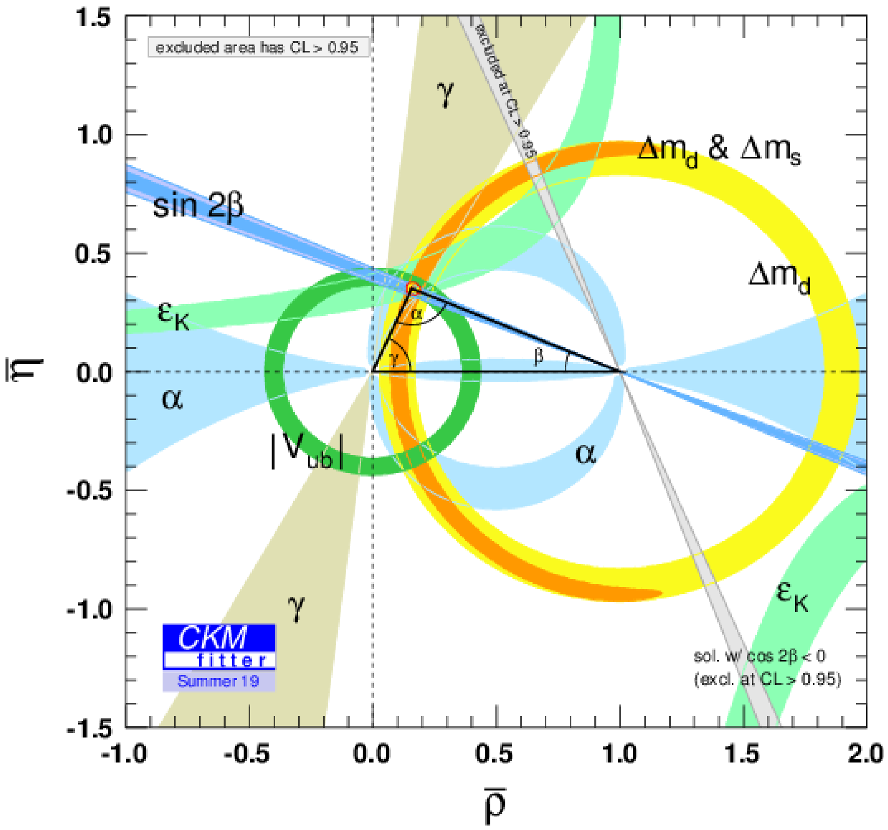

Figure 1.2: Latest CKM fit in the complex plane (Summer 2019). $\bar{\rho}$ and $\bar{\eta}$ defined as in Ref. [16]. The red dashed area near the triangle's apex with α angle is the global combination corresponding to the 68% confidence level [17].

Moreover, the unexplained discrepancy troubles the physicists as the inclusive and exclusive measurements of $|V_{ub}|$ differ, which can be seen in the Fig. 1.3.

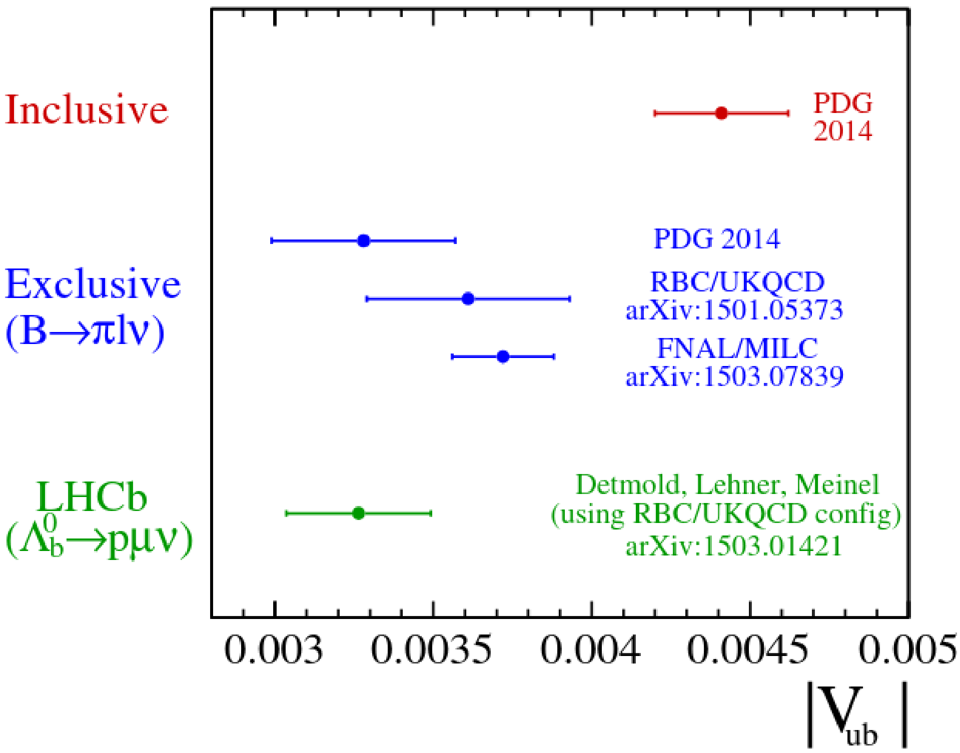

Figure 1.3: Constraints from experiments on $|V_{ub}|$, including the LHCb measurement with a baryonic decay using Run1 data set (green), showing the discrepancy between the exclusive (blue) and inclusive (red) results made by PDG [18].

BaBar collaboration performed the inclusive measurements using $\bar{B} \to X_u \ell \bar{\nu}_\ell$ and contributed to the average inclusive measurement of $|V_{ub}| = (4.25 \pm 0.12_{\text{exp}} {}^{+0.15}_{-0.14}{}_{\text{theo}} \pm 0.23) \times 10^{-3}$ [19, 20]. Exclusive measurements of LHCb, Fermilab with MILC and the RBC with UKQCD collaborations suggest the average exclusive measurement of $|V_{ub}| = (3.70 \pm 0.10 \pm 0.12) \times 10^{-3}$ [20]. Possibility to obtain new exclusive $|V_{ub}|$ measurement would give an insight into mentioned inconsistency. Therefore, investigating the branching ratio of $\Lambda_b^0 \to D_s^- p$ should be taken into consideration as it is proportional to $|V_{ub}|$, as Feynman diagram of the decay in Fig. 1.4 shows. The branching fraction of the decay $\Lambda_b^0 \to D_s^- p$ can be established as:

$$BR(\Lambda_b^0 \to D_s^- p) \propto |V_{ub}|^2 |a_{NF}|^2 f_{D_s^-}^2 F_{\Lambda_b^0 \to p}^2 (m_{D_s^-}), \tag{1.3}$$

where $f_{D_s^-}^2$ is the decay constant of the D_s^- meson and $F_{\Lambda_b^0 \to p}^2(m_{D_s^-})$ denotes the form factor of the Λ_b^0 to p decay as a function of the D_s^- meson energy. The form factor and the decay constant depend on the strong force acting between the hadrons that take part in the reaction. To describe gluon interactions between the D_s^- meson and the proton, the non-factorizable effect in the form of a_{NF} parameter was introduced. This component is yet to be accurately determined, thus not having sufficient knowledge about non-factorizable effects, measurements are described using $|V_{ub}| \times |a_{NF}|$. The

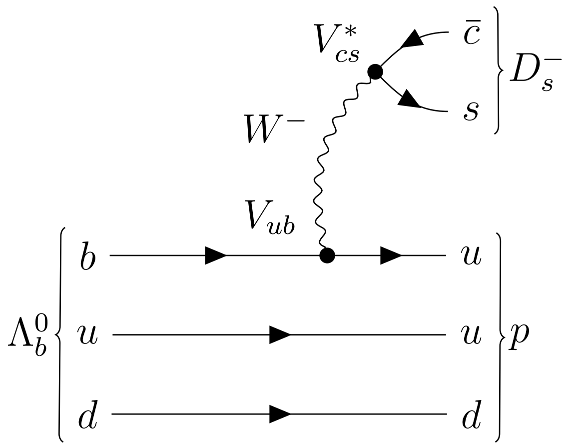

Figure 1.4: The Feynman diagram of the decay $\Lambda_b^0 \to D_s^- p$.

$\Lambda_b^0 \to D_s^- p$ decay constitutes a background to other analyses, e.g. the study of CP violation with $B_s^0 \to D_s^\mp K^\pm$ decays [21], where the yield of $\Lambda_b^0 \to D_s^- p$ is one of the contributing backgrounds to the signal region. In addition, the comparison can be made between non-factorizable effects of the $\Lambda_b^0 \to D_s^- p$ and B meson decays.

In order to obtain the branching fraction, the yield of $\Lambda_b^0 \to D_s^- p$ must be determined. The specific case for D_s^- meson decay as $D_s^- \to K^- K^+ \pi^-$ was chosen. The known decay $\overline{\Lambda}_b^0 \to \overline{\Lambda}_c^- \pi^+$, where $\overline{\Lambda}_c^-$ baryon decays in the form of $\overline{\Lambda}_c^- \to \overline{p} K^+ \pi^-$, was used for normalisation in the branching fraction, as this choice minimises possible sources of systematic uncertainty associated to the measurement. Thus to estimate the branching ratio of $\Lambda_b^0 \to D_s^- p$, one shall proceed to obtain the factors in the Eq. (1.4):

$$
\begin{aligned}
\frac{BR(\Lambda_b^0 \to D_s^- p)}{BR(\overline{\Lambda}_b^0 \to \overline{\Lambda}_c^- \pi^+)} &= \frac{N(\Lambda_b^0 \to (D_s^- \to K^- K^+ \pi^-) p)}{N(\overline{\Lambda}_b^0 \to (\overline{\Lambda}_c^- \to \overline{p} K^+ \pi^-) \pi^+)} \times \\
&\times \frac{\epsilon(\overline{\Lambda}_b^0 \to (\overline{\Lambda}_c^- \to \overline{p} K^+ \pi^-) \pi^+)}{\epsilon(\Lambda_b^0 \to (D_s^- \to K^- K^+ \pi^-) p)} \times \frac{BR(\overline{\Lambda}_c^- \to \overline{p} K^+ \pi^-)}{BR(D_s^- \to K^- K^+ \pi^-)},
\end{aligned}
\tag{1.4}
$$

where N denotes the specific decay yield, ϵ is the specific decay detection efficiency and BR stands for the branching fraction of the decay. Such normalisation mode was chosen because of a similar topology of both decays, where a charmed hadron decays into three other hadrons accompanied by a companion particle (e.g. for $\Lambda_b^0 \to D_s^- p$, it is p). For this thesis, when mentioning a particular decay type, the charged conjugated decay is also included (e.g. for $\Lambda_b^0 \to D_s^- p$ this method concerns $\overline{\Lambda}_b^0 \to D_s^+ \overline{p}$).

The main goal of this thesis is to estimate yields of the decays in interest, which together with the efficiency information can be used to perform the first branching ratio of the $\Lambda_b^0 \to D_s^- p$ to $\overline{\Lambda}_b^0 \to \overline{\Lambda}_c^- \pi^+$ decay.

Chapter 2

The LHC experiment

The Large Hadron Collider (LHC), build at European Council for Nuclear Research (CERN) near Geneva, Switzerland is the most sophisticated tool modern Particle Physics has to offer. This particle collider is designed for the analysis of the proton collisions, but the case of lead-lead collisions can also be examined. The LHC is a two-ring synchrotron build in a circular tunnel, almost 27 km in circumference, located approximately 100 m under the ground level, in place of previously active LEP experiment. The designed center-of-mass energy for protons in the LHC takes the value of 14 TeV [22]. The LHC experimental programme follows a well-planned series of data taking periods with technical stops for repairing and upgrading the accelerators and detectors, and the final step being the major transformation of the LHC to the High Luminosity-Large Hadron Collider (HL-LHC) in 2024-2026, introducing injector upgrades for luminosity levelling [23]. The Fig. 2.1 pictures the roadmap showing values of luminosity and center-of-mass energy available for proton collisions in LHC, for the past, present and the future plans, not including the delay associated with the global pandemic in 2020.

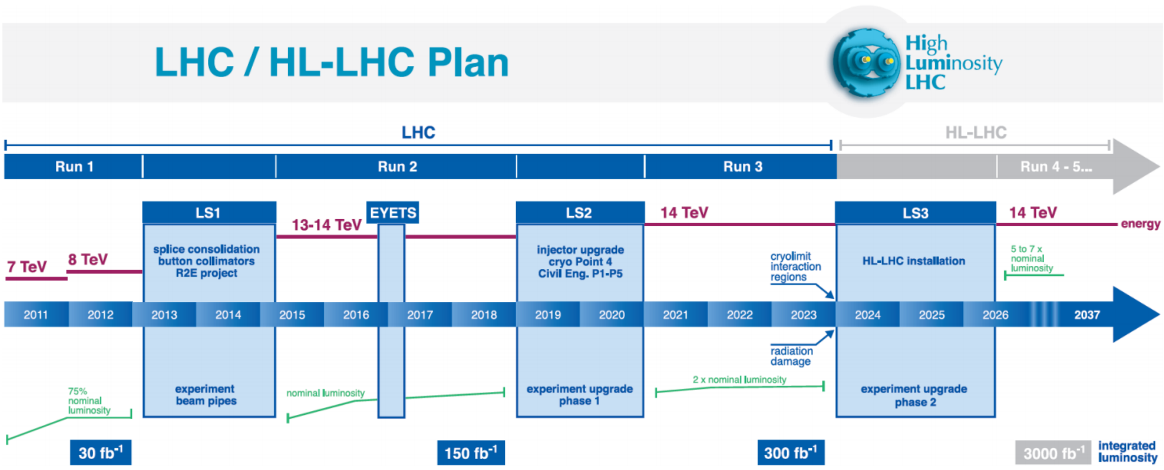

Figure 2.1: Timeline of the LHC programme up to the high-luminosity LHC (HL-LHC), with luminosity and center-of-mass energy values for each year of data taking. Periods of long shutdowns for upgrades are denoted as LS, while those of data taking - as Runs [23].

In order to understand, why the measurements at LHC have to be planned in advance, it is convenient to dive into the structure of LHC and accompanied experiments, to see the level of complexity physicists have to deal with. Before the particles are set to travel inside the Large Hadron Collider, symbolically drawn in the Fig. 2.2, they gain momentum thanks to the system build out of several smaller accelerators and synchrotrons.

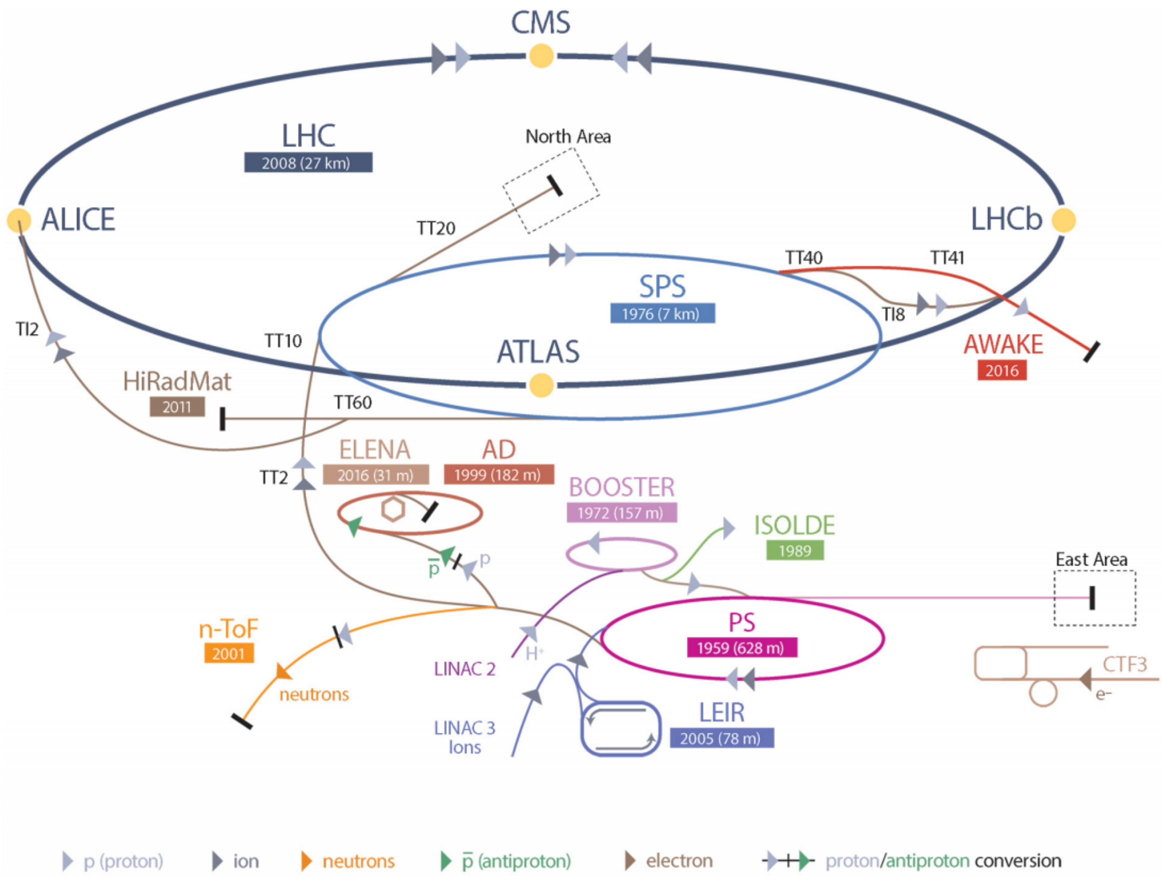

Figure 2.2: Scheme of LHC accelerator and synchrotron complex [23].

Particles are accelerated to increasingly higher energies and the beams in which they travel are being formed by the means of many different machines. Each one of them contributes to the beam energy and in the next step inject the beam into the next system. For the case of protons, they are accelerated to 50 MeV in the Linac 2, 1.4 GeV in the PS Booster (violet colour in Fig. 2.2), 26 GeV in the Proton Synchrotron PS (pink) simultaneously forming spatial proton bunches with 25 ns distance between each bunch. These bunch trains move to the SPS, Super Proton Synchrotron (light blue) where they gain energy up to 450 GeV before being injected into the two separate rings in LHC in opposite directions. For every part of acceleration process, fractions of the beams, with energies corresponding to the energy limits of the accelerator from which they left, are used in fixed target experiments. The rest goes into the superconducting proton/ion accelerator and collider of LHC in the underground tunnel with 4 m diameter in cross-section [23].

The Large Hadron Collider governs four major specialised experiments with general purpose detectors:

- ATLAS [24] and CMS [25] - the largest of them all, used for studies of various physics areas as they are the most versatile with excellent jet and missing transverse momentum resolution, particle identification, muon measurement and flavour tagging;

- ALICE [26] for detection of gluon-plasma interactions where it distinguishes itself among other experiments with excellent track reconstruction in environment of heavy ions;

- the LHCb detector [27] designed to study the differences in matter and antimatter behaviour in particle interactions by examining issue of CP violation in hadronic sector, especially for particles with b or c quarks.

Having in mind that layout of the LHC was adapted to follow the already existing tunnel for LEP, eight arcs and eight straight sections can be distinguished. The straight sections have approximately 528 m in length and were designed to allow for insertions. The layout of the LHC, with distinction between octants and Points in the middle of each one, with detectors and beam aparatus positions is shown in Fig. 2.3. At two diametrically opposite straight sections high luminosity insertions for experiments are set: the ATLAS experiment at IP 1 and the CMS at IP 5. Points 2 and 8 correspond to ALICE and LHCb placement with injection systems for two beams. Remaining four straight sections do not contain any beam crossing points, while unmentioned Points constitute place for the beam controlling systems [22].

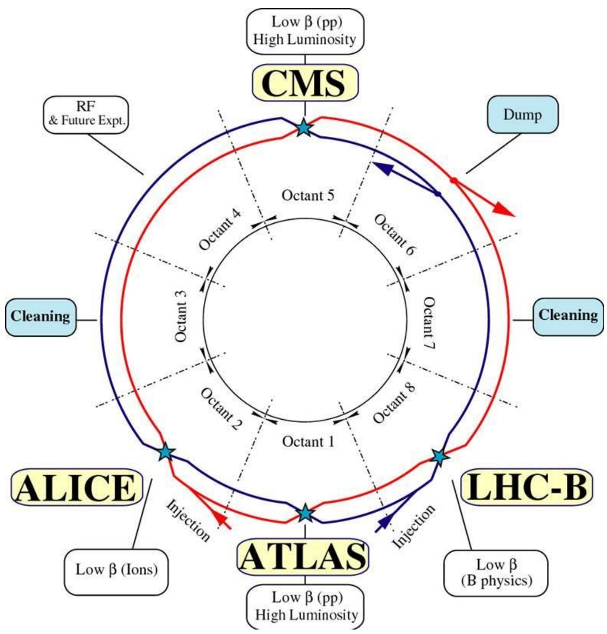

Figure 2.3: The Large Hadron Collider layout with the beam processes included [28].

2.1. The LHCb detector

The LHCb detector was dedicated to study heavy flavour physics, look for indirect new physics evidence in area of CP violation as well as rare beauty and charm hadron decays [27]. One of the most distinguishable properties of beauty hadrons is the fact that, for high energies, produced particles outgo the same forward or background cone along the beamline direction.

What describes LHCb best is naming it a single-arm forward spectrometer. It is located in the Intersection Point 8 of the LHC, previously used by the DELPHI experiment when LEP was still operational, with the interaction point not located at the center of the cavern, but at its side (11.25 m from the middle of the hall). This setup enables detection of the particles going out of one side of the collisions only, with a low impact parameter (outgoing the interaction region close to the beamline), thus it is perfect for beauty physics studies. LHCb covers angles up to 250 mrad in non-bending plane and the pseudorapidity $\eta \in [2; 5]$, for η equal to $-\ln(\tan(\theta/2))$, where θ is the polar angle measured from the positive z axis (along the beam direction) [27]. In its coordinate system, which is right-handed with y axis along the vertical, the beamline is parallel to the direction towards positive z axis. Fig. 2.4 shows the side schematic view of the LHCb detector, with its coordinate system and several subdetectors.

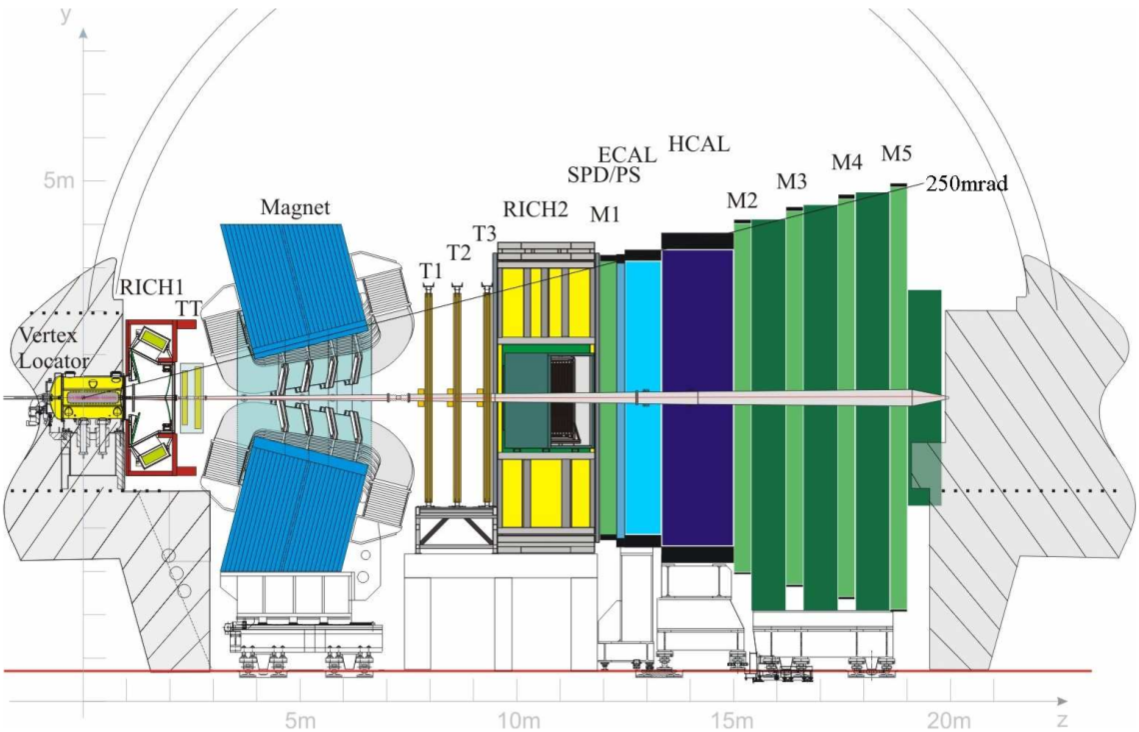

Figure 2.4: LHCb detector structure in yz plane, operational for Run1 and Run2 [29].

In order to comprehend how LHCb is able to gather unprecedented amount of data describing beauty hadrons, it is necessary to gain insight into its systems. The detector consists of many subdetectors which aim to register the flight path of the particles (tracking) and to identify them (PID). The following descriptions concern the state of LHCb detector in years 2010-2018.

2.1.1. Tracking

The B-meson lifetime is approximately 1.5 ps at the LHC framework, which translates to the average distance covered by this particle of about 1 cm. Thus the high precision tracking system is necessary to determine the position of primary and secondary interaction vertices [30].

Three subdetectors for the tracking can be distinguished. The one closest to the beamline and the interaction point (only 8 mm from the beam pipe) is the Vertex Locator VELO, which simplified diagram is shown in Fig. 2.5. It consists of silicon modules, that provide the r and ϕ coordinates measurements along the beam direction for the passing particles.

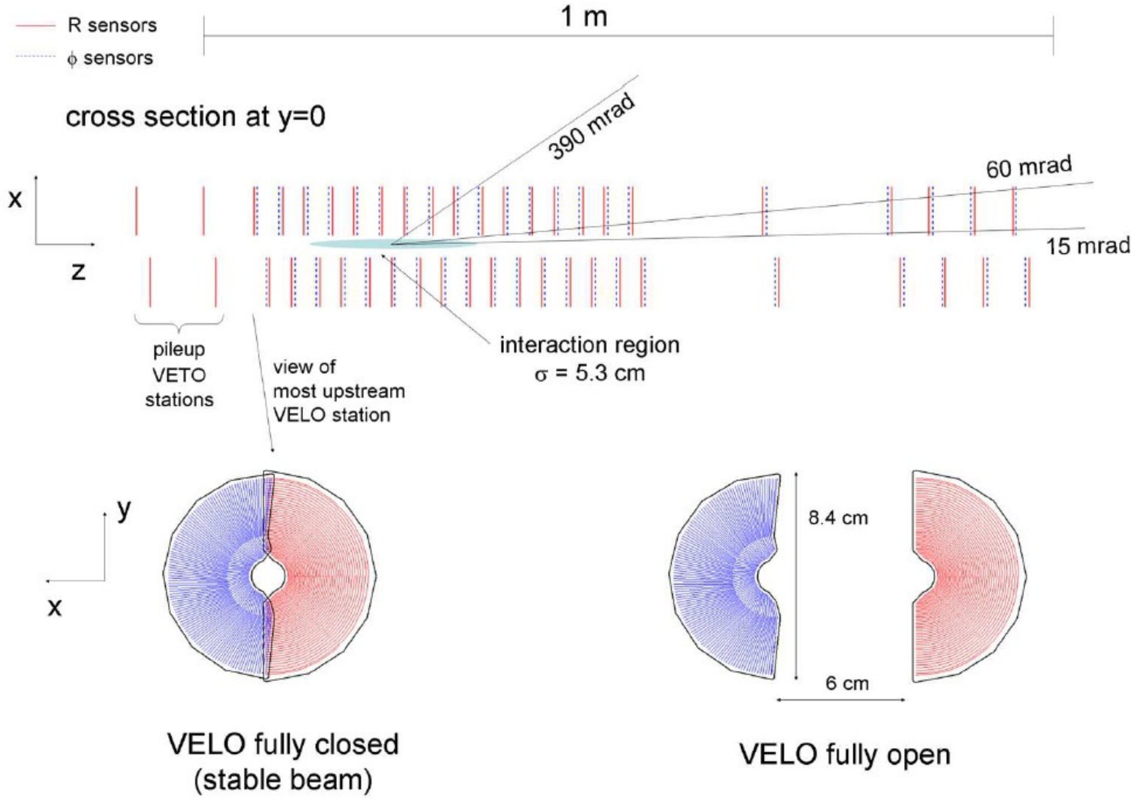

Figure 2.5: Cross-section in the xz plane of the VELO silicon sensors, at $y = 0$, with the detector in the fully closed position. The front face of the first modules is also illustrated in both the closed and open positions [27].

The modules are mounted in a vessel that preserves vacuum around the sensors and is separated from the beamline vacuum by a thin walled aluminum sheet. This way charged particle traverses minimal material before sensors crossing. Moreover, two halves of the VELO can overlap in closed position, so that the full ϕ angular coverage is provided.

Another part of the tracking system is the Silicon Tracker (ST), comprised of four stations: the Tracker Turicensis (TT) located upstream the magnet [31, 32] and the three tracking stations T1, T2 and T3 downstream the magnet, which are composed of Inner Tracker (IT) [33] and Outer Tracker OT [34]. Every each of them use silicon microstrip sensors with a strip pitch under 200 μm. TT covers the full acceptance of the detector, while the IT is arranged in a cross formation in the middle of each of the three tracking station (T1, T2 and T3), which location in LHCb can be seen in Fig. 2.4. The four ST stations have detection layers arrangement with vertical strips in the first and second layer and strips rotated by a stereo angle of $\mp 5°$ in, correspondingly, the second and third layer (denoted $xu\nu x$). This way, a better spatial resolution of particle tracks can be convoluted [27]. Fig. 2.6 shows an example of rotated sensors for a scheme of four detection layers that TT possess.

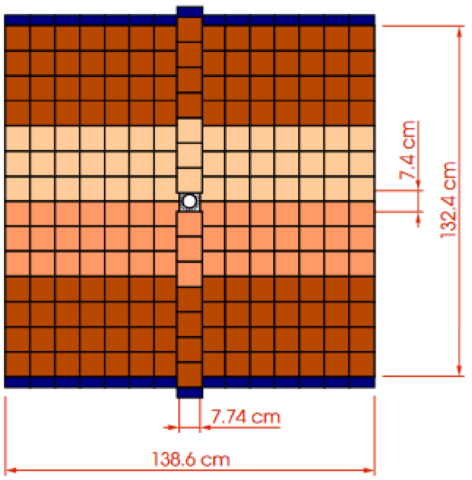

(1st detection layer)

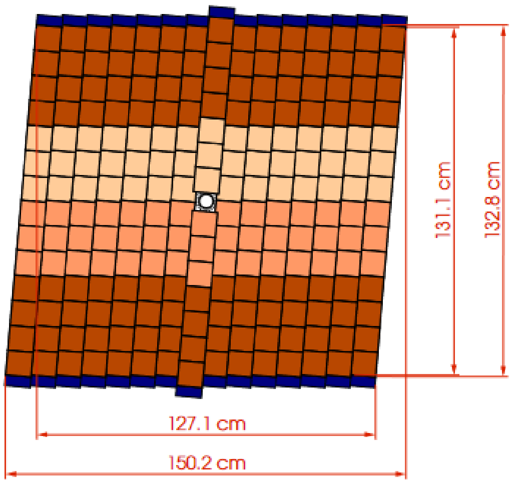

(2nd detection layer)

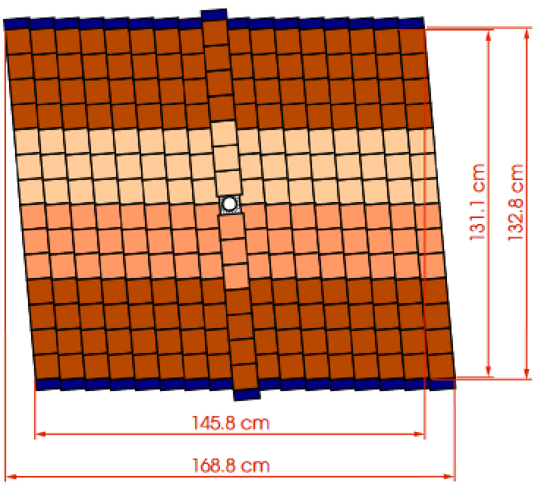

(3rd detection layer)

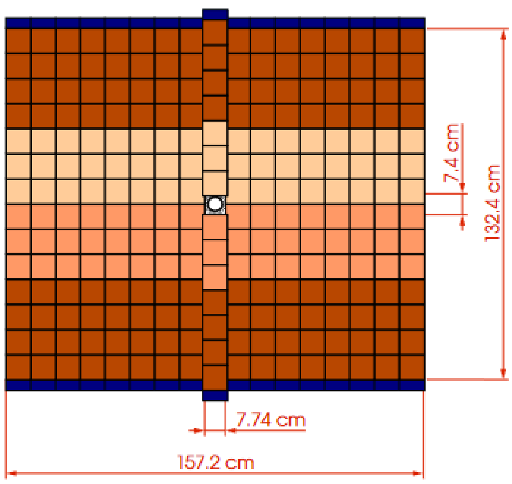

(4th detection layer)

Figure 2.6: Layout of the four detection layers of the TT station. Different shading indicates the different readout sectors along the silicon ladder [32].

The third element of tracking systems is the Outer Tracker OT, which is the array of separate gas-tight straw-tube modules. The OT modules together with the IT create tracking stations T1, T2, T3. Fig. 2.7 shows the setup in which they are combined for a separate station.

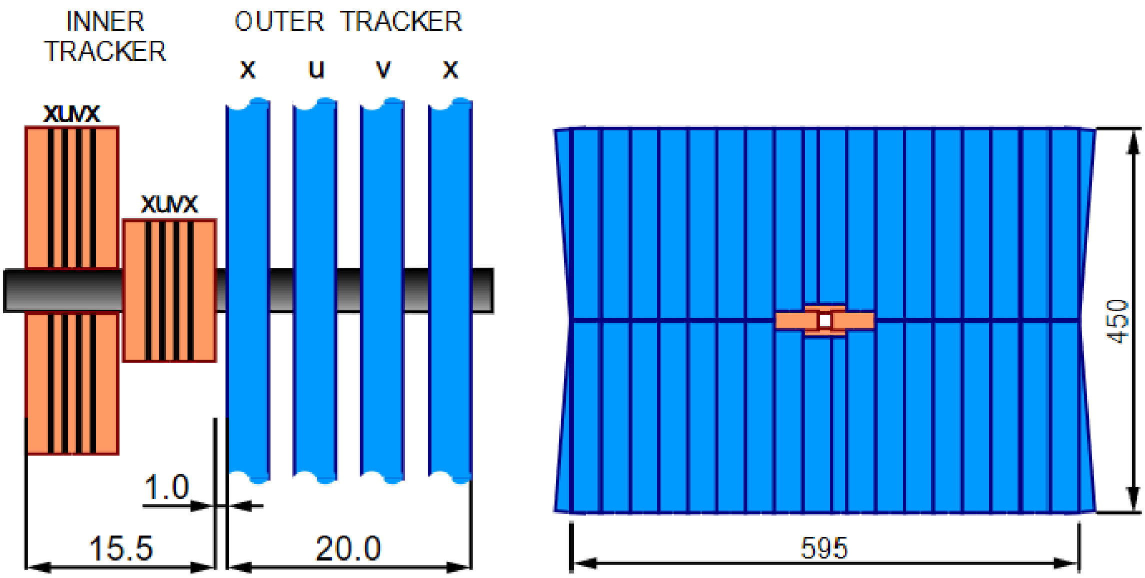

Figure 2.7: Left: Tracking station as seen from the top. Lateral dimensions are not to scale. Right: Front view of a tracking station. All dimensions are given in cm [33].

This mixture of systems provide fast drift time (less than 50 ns) and drift-coordinate resolution of the order of 200 μm, thus the LHCb is capable of determining the particle's momentum with a relative uncertainty up to 0.5% for momenta below 20 GeV/c and 0.8% at the order of 100 GeV/c [35].

An important fact is that in between tracking stations the magnet is placed, which allows for track bending for charged particles. Its integrated filed strength is 4 Tm and thanks to the fact that it can switch polarity, physicists get rid of any bias from polarization in the measured data. In data samples that were considered, this was included in the cases $MagUp$ and $MagDown$.

2.1.2. Particle Identification (PID)

Many LHCb detector systems allow for particles to be identified. Among them, two Ring Imaging CHerenkov Counters (RICH1 and 2) play a significant role - they detect the Cherenkov radiation that is emitted by a charged particle passing through the detector material with a speed exceeding the speed of light in that material c', given by a formula:

$$c' = \frac{c}{n},$$

where n is the refractive index of the medium and c is the light speed in vacuum.

Value of the so-called Cherenkov angle θ_C, in which the particle emits radiation in relation to the direction of its propagation, is related to the particle's velocity v, according to the formula:

$$\cos(\theta_C) = \frac{c'}{v} = \frac{1}{\beta n}, \tag{2.1}$$

for β equal v/c. Therefore, if the Cherenkov angle is measured, the information about the v is determined, that combined with momentum measurement from detectors of the tracking system can give an estimation of the particle's mass. This results in a particle identification.

Several gases are suitable for distinguishing particles for low- and high-momenta measurements, as can be seen in Fig. 2.8.

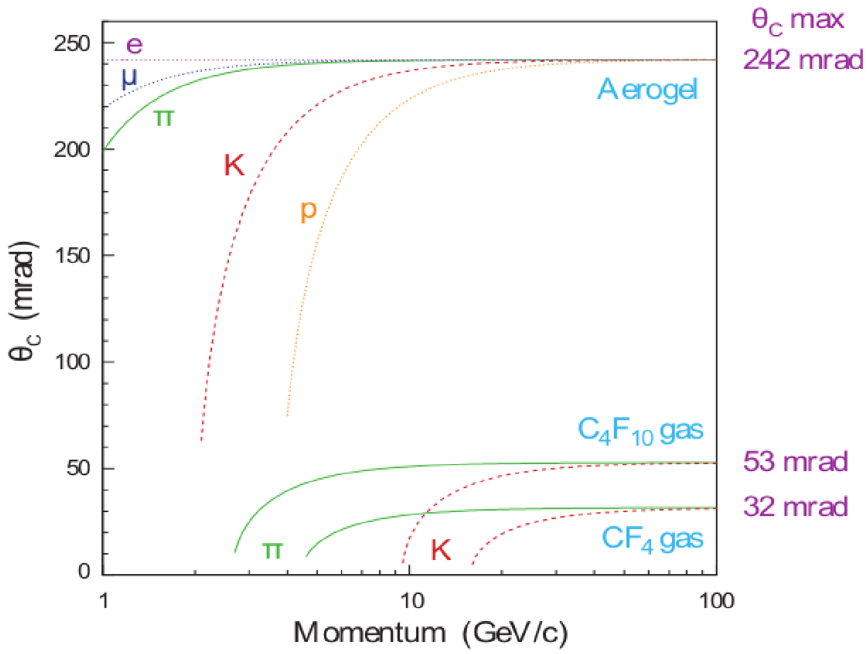

Figure 2.8: Cherenkov angle θ_C versus track momentum for different particles and radiators [27].

As the figure suggests, to assure correct particle identification over a broad range of momenta, more then one type of radiators must be used. Thus materials filling the RICH detectors are silica aerogel and C_4F_{10} for RICH1, aiming for the lower-momenta particles, while for RICH2, designed to measure particles with higher momenta, it is CF_4 [27]. Fig. 2.9 depicts the RICH's designs.

The light, that is emitted by the particles traversing RICH, is collected by flat spherical mirrors and reflected onto the photomultiplier tubes and Hybrid Photo Detectors (HPDs), from where the information about the detection could be passed on.

Not every particle is both heavy and charged, e.g. photons, electrons and hadrons. Thus LHCb possess Electromagnetic and Hadronic Calorimeters (ECAL and HCAL) that can measure energy of these objects. Their method of work is simple: particle traversing the detector interacts with the absorber material, creating a secondary shower (electromagnetic and/or hadronic). This shower can be measured, by gathering the emitted light and/or electric charge, thanks to the scintillators and silicon detectors. Passing by, charged particles and photons leave energy deposits that are recorded thanks to the ECAL, while for charged and neutral hadrons, this function is fulfilled by the HCAL. For the lowest trigger, $\Lambda_b^0 \rightarrow D_s^- p$ decays can be found amongst the incoming flood of data, thanks to the calorimeters.

The last system used for particle identification is the system of five muon stations (M1-M5) of rectangular shape, placed along the beam axis that provide fast information about the high transverse momenta muons. The muon system is highly efficient

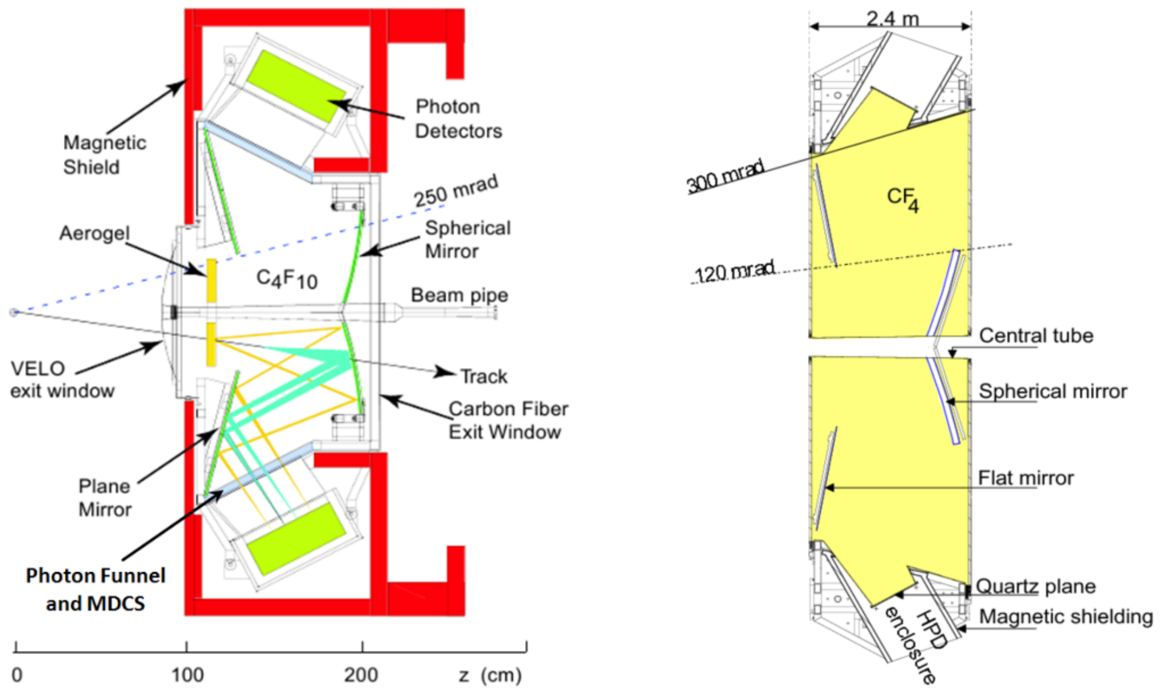

Figure 2.9: Layout of the LHCb Ring Imaging Cherenkov detectors: RICH1 (on the left) and RICH2 (on the right) [27].

at detecting muons as almost all other particles are caught by ECAL and HCAL beforehand.

For the LHCb framework, to properly combine results from all the sub-detectors, each charged particle that is reconstructed is assigned a likelihood of being a particle of certain type, e.g. a kaon, a pion or a proton. To do that, the difference in logarithmic likelihood is defined, as $\mathrm{DLL(A-B)} = \ln\mathcal{L}_\mathrm{A} - \ln\mathcal{L}_\mathrm{B}$, where $\mathcal{L}_\mathrm{A}$ and $\mathcal{L}_\mathrm{B}$ are the likelihoods of a particle being identified under A and B hypotheses. That means, for DLL(A-B) <0, the particle is more likely to be of B type, while for DLL(A-B) >0, the opposite statement is true.

For the $B_s^0 \to D_s^-\pi^+$ and $B_s^0 \to D_s^\mp K^\pm$ decays, the final state particles are kaons and pions. To correctly separate these channels, the correct identification must be done. There is certain probability of a pion being misidentified as a kaon, thus the distinction between these two is important for the analysis. The crucial variable is PIDK, defined as:

$$\mathrm{PIDK} = \mathrm{DLL}(K-\pi), \tag{2.2}$$

where a particle is reconstructed under either kaon or pion-like hypotheses (either a pion or a ρ meson).

The issue of different particles, e.g. a proton, that is one of the final state particles for the $\Lambda_b^0 \to D_s^- p$ decay, may be resolved thanks to the ProbNNp variable that comes from the trained neural network and allows for determining whether a particle is a proton, amongst all other particles [36]. This behaviour of both statistical methods makes the procedure perfect for $\Lambda_b^0 \to D_s^- p$ studies.

Chapter 3

The $\Lambda_b^0 \to D_s^- p$ analysis

The data taking periods at LHC are limited due to the fact that scientific equipment needs maintenance. The description of the Large Hadron Collider timeline was presented in Fig. 2.1. First measurements have been conducted in years 2011 and 2012, the time called Run1. In 2013 and 2014 the detectors have been modified for Run2 so that the detector could gather unprecedented amount of data in 2015-2018. From that point, the next long shutdown is now taking place and is up to end this year (with a slight delay because of the global pandemic). For this analysis, the data collected in Run1 and Run2 are analysed. The luminosity values for each year with the magnet polarity are listed in Table 3.1.

Table 3.1: Intergated luminosity split by year of data taking and the magnet polarity expressed in fb^{-1}.

Sample	2011	2012	2015	2016	2017	2018
Magnet down	0.56	0.99	0.19	0.86	0.88	1.05
Magnet up	0.42	1.00	0.15	0.81	0.83	1.14
Both	0.98	1.99	0.33	1.67	1.71	2.19

The previous work of the $\Lambda_b^0 \to D_s^- p$ decays has not been published, but was performed as Polish-Dutch collaboration with NIKHEF group and was a subject of another Master Thesis dissertation [37]. Since then the data set has been extended to the full Run2 period, the selection has been re-optimised to minimise systematic uncertainties. This required re-processing of all samples. In addition, a data-driven approach of background estimation from control modes, the $B_s^0 \to D_s^- \pi^+$ and $B_s^0 \to D_s^\mp K^\pm$ channels, has been proposed by the Polish part of the analysis.

Such LHCb official samples of data and simulation are part of the studies:

- $B_s^0 \to D_s^\mp K^\pm$ control mode;
- $B_s^0 \to D_s^- \pi^+$ control mode;
- $\overline{\Lambda}_b^0 \to \overline{\Lambda}_c^- \pi^+$ normalisation decay;
- $\Lambda_b^0 \to D_s^- p$ signal decay.

All four samples are statistically independent. The reason why three other decay channels are studied if the main topic of interest for this work is the $\Lambda_b^0 \to D_s^- p$ channel is that all mentioned decays have similar kinematic properties as there are four particles in the final state and a flavour transition - from beauty to charm quark - which result in related properties of their primary and secondary vertices and thus high probability of mixing up decays with one another. Thus, usage of the $B_s^0 \to D_s^\mp K^\pm$ and $B_s^0 \to D_s^- \pi^+$ samples allows for the data-driven way of estimating background contributions in the $\Lambda_b^0 \to D_s^- p$ sample.

3.1. Methodology

For this work, the decays with a structure $B \to Dh$, $D \to hhh$ are considered, which simplified topology is shown in Fig. 3.1, as $\Lambda_b^0 \to D_s^- p$ decay follows this decay chain. In $B \to Dh$ decays a meson or a baryon with a beauty quark, denoted B (cyan), decays into a meson or a baryon with a charm quark, D (orange) and an additional particle h (violet). Later on, as the charm particle D is not stable, it produces three other particles, also denoted h (red). The picture additionally shows the impact parameter (IP) and flight distance (FD), in green and light blue colours with the primary vertex (PV) depicted as a star. The definitions of all the introduced observables are noted in App. A.

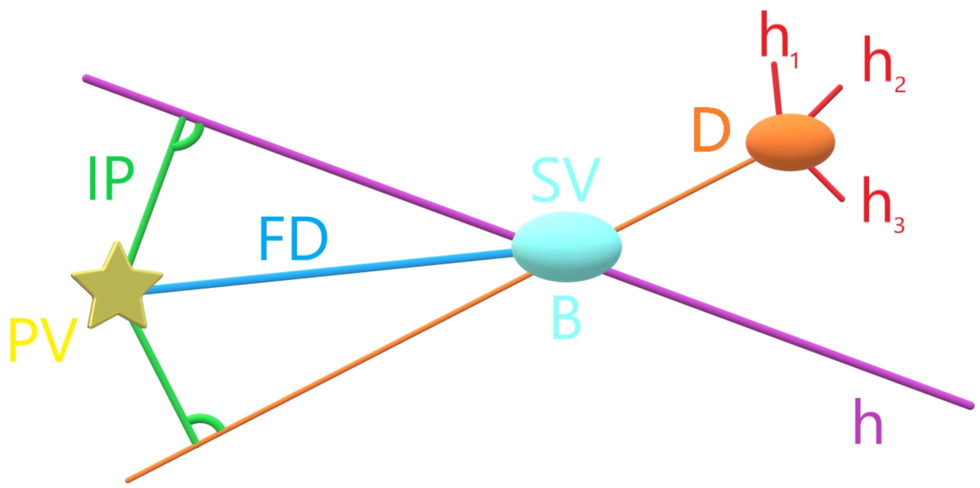

Figure 3.1: The symbolic spatial diagram of the beauty to charm particle decay denoted $B \to Dh$ with additional kinematic parameters. Their definitions are written in App. A.

The similarity among all mentioned decays can be seen as in place of the beauty particle B either Λ_b^0 baryon or a B_s^0 meson are considered and for charm particle D these are either $\bar{\Lambda}_c^-$ or D_s^-. The additional h particle, called the companion, is in the case of this analysis a proton p, while for other decays a pion π or a kaon K. Charm candidate D is not stable and decays further to other particles, for $\Lambda_b^0 \to D_s^- p$ the decay $D_s^- \to K^- K^+ \pi^-$ is considered, and that property has to be included in analysis too. By that manner, for the proper understanding of eventual misidentification of one decay channel similar to another, the decay channels similar to $\Lambda_b^0 \to D_s^- p$ must be compared. The decay chains of $\Lambda_b^0 \to D_s^- p$ and others, considered in the analysis, are written in Table 3.2. Table 3.3 additionally shows the values of branching fractions for these decays with f_s/f_d ratio of B_s^0 to B^0 meson production cross-sections in LHCb. In addition, in a separate Table 3.4 the properties of mentioned particles are listed.

Table 3.2: Decays considered in the analysis.

Beauty to charm decay (former)	Charm decay (latter)
$\Lambda_b^0 \to D_s^- p$	$D_s^- \to K^- K^+ \pi^-$
$B_s^0 \to D_s^- \pi^+$	$D_s^- \to K^- K^+ \pi^-$
$B_s^0 \to D_s^\mp K^\pm$	$D_s^- \to K^- K^+ \pi^-$
$\overline{\Lambda}_b^0 \to \overline{\Lambda}_c^- \pi^+$	$\overline{\Lambda}_c^- \to \overline{p} K^+ \pi^-$

Table 3.3: The branching fractions are taken from the PDG [38], while f_s/f_d is the LHCb hadronic/semi-leptonic combination [39].

Channel	Branching fraction
$B_s^0 \to D_s^- \pi^+$	$(3.04 \pm 0.23) \times 10^{-3}$
$B_s^0 \to D_s^\mp K^\pm$	$(0.23 \pm 0.02) \times 10^{-3}$
$B^0 \to D^- \pi^+$	$(2.57 \pm 0.13) \times 10^{-3}$
$\overline{\Lambda}_b^0 \to \overline{\Lambda}_c^- \pi^+$	$(4.9 \pm 0.4) \times 10^{-3}$
$D_s^- \to K^- K^+ \pi^-$	$(5.45 \pm 0.17) \times 10^{-2}$
$D_s^- \to \pi^- \pi^+ \pi^-$	$(1.09 \pm 0.05) \times 10^{-2}$
$D^- \to K^+ \pi^- \pi^-$	$(9.38 \pm 0.16) \times 10^{-2}$
$\overline{\Lambda}_c^- \to \overline{p} K^+ \pi^-$	$(6.28 \pm 0.32) \times 10^{-2}$
f_s/f_d	$0.259 \pm 0.015($ (stat)& (syst))

Table 3.4: Properties of the particles, as given by PDG [38].

Particle	Quark composition	Mass [MeV/c^2]	Lifetime	Spin
Λ_b^0	udb	5619.60 ± 0.17	(1.471 ± 0.009) ps	1/2
B_s^0	$s\bar{b}$	5366.88 ± 0.14	(1.515 ± 0.004) ps	0
B^0	$d\bar{b}$	5279.65 ± 0.12	(1.519 ± 0.004) ps	0
$\bar{\Lambda}_c^-$	$\bar{u}\bar{d}\bar{c}$	2286.46 ± 0.14	(202.4 ± 3.1) fs	1/2
D_s^-	$s\bar{c}$	1968.34 ± 0.07	(504 ± 4) fs	0
D^-	$d\bar{c}$	1869.65 ± 0.05	(1040 ± 7) fs	0
p	uud	938.272081 ± 0.000006	$> 3.6 \times 10^{29}$ years	1/2
K^+	$u\bar{s}$	493.677 ± 0.016	(12.38 ± 0.02) ns	0
π^+	$u\bar{d}$	139.57039 ± 0.00018	(26.033 ± 0.005) ns	0

For the particles mentioned, the corresponding antiparticles have the same properties except for the opposite electric charge and the quark composition, with all the quarks exchanged to their antimatter partner (and vice versa).

To understand, why the decays in Table 3.2 can be mismatched, thus what is the reason for the two decay channels (except for the $\overline{\Lambda}_b^0 \to \overline{\Lambda}_c^- \pi^+$ as it is a normalisation channel) to be considered as part of a background for $\Lambda_b^0 \to D_s^- p$ in the analysis, the concept of the decay hypothesis is explained.

Every decay might be reconstructed on the basis of its own hypothesis as well as other decay hypothesis, for example:

- $B_s^0 \to D_s^{\mp} K^{\pm}$ under self hypothesis $B_s^0 \to D_s^{\mp} K^{\pm}$;
- $B_s^0 \to D_s^{\mp} K^{\pm}$ under hypothesis of the decay $B_s^0 \to D_s^- \pi^+$ or $\Lambda_b^0 \to D_s^- p$, in which case kaon K^+ changes its mass hypothesis to mass of a pion π^+ or a proton p.

Using the official LHCb simulation sample of $B_s^0 \to D_s^- \pi^+$ decay, a comparison of the invariant mass of $D_s^- \pi^+$ pair for the decay $B_s^0 \to D_s^- \pi^+$, $D_s^- \to K^- K^+ \pi^-$ under its own hypothesis and the $B_s^0 \to D_s^{\mp} K^{\pm}$, $D_s^- \to K^- K^+ \pi^-$ decay hypothesis is made. The result is shown in Fig. 3.2.

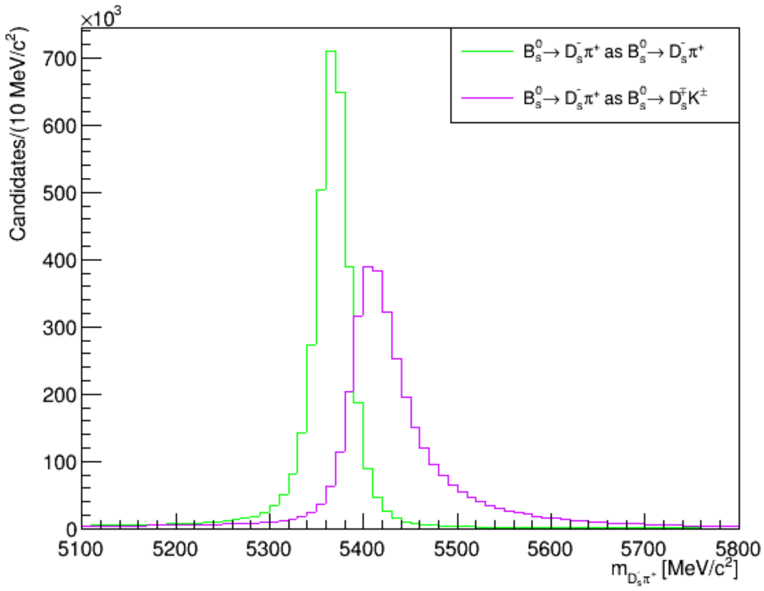

Figure 3.2: $D_s^- \pi^+$ invariant mass $m_{D_s^- \pi^+}$ distributions for the decay $B_s^0 \to D_s^- \pi^+$ under its own hypothesis (green colour), as well as the decay hypothesis of $B_s^0 \to D_s^{\mp} K^{\pm}$, $D_s^- \to K^- K^+ \pi^-$ (violet colour). The plot is based on the official LHCb simulation sample, for 2016, magnet down polarity ($MagDown$).

The fact that different hypotheses have to be considered for the invariant mass analysis is a consequence of incapability of saying with a 100% confidence level whether the particle reconstructed from the experimental data is a pion, a kaon or whether it was misidentified. Because of that, for example, a pion might be misidentified as a kaon which would result in a shift in the invariant mass distribution of $D_s^- \pi^+$, reconstructed using a heavier particle, towards greater values. This behaviour, as it would be thought, is non linear, because the higher mass values of B_s^0 would more often correspond to the $D_s^{\mp} K^{\pm}$ variant, while for the lower values this behaviour would opt for $D_s^- \pi^+$. Thus whole distribution changes, even in mid-ranges. For the $D_s^{\mp} K^{\pm}$ variant, the distribution shifts towards the higher invariant mass values than for $D_s^- \pi^+$.

Going back to $\Lambda_b^0 \to D_s^- p$, to obtain its yield, one must first estimate yields of other decays, that might find themselves in the signal window through the misidentification of the outgoing particles. To do that, a data-driven approach is used, as it is schematically shown in Fig. 3.3:

- the $B_s^0 \to D_s^- \pi^+$ sample: the invariant mass fit to the $m(D_s^- \pi^+)$ distribution is performed after requiring PIDK<0 (see Eq. (2.2)) on the companion track. The yields of $B_s^0 \to D_s^- \pi^+$, $B_s^0 \to D_s^- \rho^+$, $B_s^0 \to D_s^{*-} \pi^+$ and $B_s^0 \to D_s^{*-} \rho^+$ are estimated and used later as constraints on $D_s^- \pi^+$-like background in other channels (red colour in the Fig. 3.3);
- the $B_s^0 \to D_s^\mp K^\pm$ sample: the invariant mass fit to the $m(D_s^\mp K^\pm)$ distribution is performed with a requirement PIDK>10 on the companion track (identifying it as a kaon). In the fit a remaining amount of the $D_s^- \pi$-like background is constrained from the previous step. This results in the $B_s^0 \to D_s^\mp K^\pm$, $B_s^0 \to D_s^\mp K^{*\pm}$, $B_s^0 \to D_s^{*\mp} K^\pm$, $B_s^0 \to D_s^{*\mp} K^{*\pm}$ and $B^0 \to D_s^- K^+$ (blue colour) yields estimation, called $D_s^\mp K^\pm$-like backgrounds, which are used in calculation of these contributions in the signal $\Lambda_b^0 \to D_s^- p$ sample;
- thanks to the information from both steps the background contributions in the $m(D_s^- p)$ distribution can be established, making the fit more stable and accurate (yellow colour).

For the ratio of branching fractions calculations, as in Eq. (1.4), the yield of normalisation decay $\bar{\Lambda}_b^0 \to \bar{\Lambda}_c^- \pi^+$ is also estimated (green colour in the Fig. 3.3).

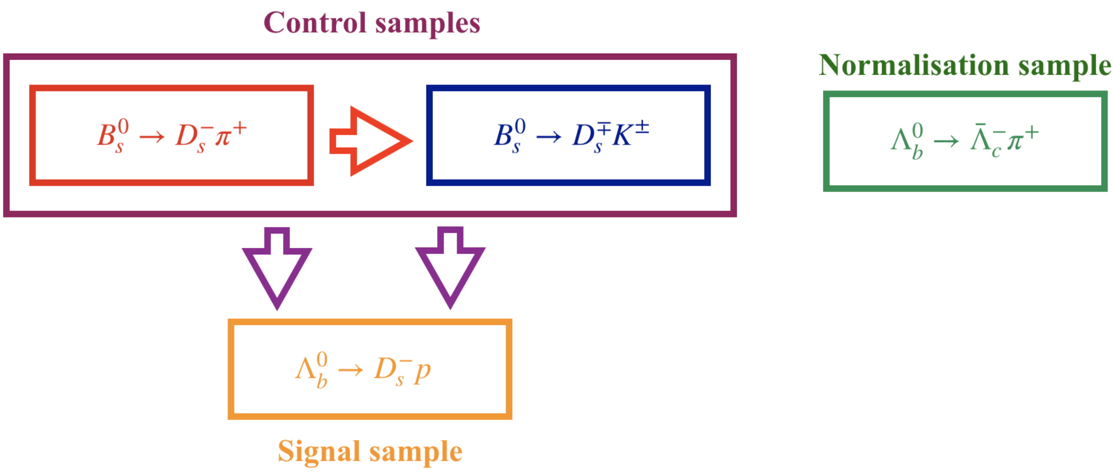

Figure 3.3: The symbolic idea of the analysis, with information flow drawn as arrows.

3.2. The background components

In general, many processes may contribute to the decay being badly identified, some of which constitute backgrounds for analysed samples. Three different kinds of these elements can be established:

- Misidentified backgrounds: as already mentioned, one of the daughter particle is misidentified (example on page 26);
- Partially reconstructed backgrounds: concern events where a parent particle decays to the daughter particle which is in an excited state. They can emit a photon γ or a neutral pion π^0. These products are not reconstructed and thus the obtained energy for the decay is lower than in reality, shifting the invariant mass to smaller values;
- Combinatorial background: caused by a coincidental grouping of particles matched as a signal. This may be either a charm D hadron paired with a random track or a random composition of final particles forming a fake D hadron reconstructed with a true companion particle. The BDT cut dismisses most of this background, but it is not 100% efficient, thus, in general, the combinatorial background has to be considered in the analysis.

The simulation samples are used for the study of the misidentified and partially reconstructed backgrounds. The combinatorial background shape is exterminated using the mass fit in the range out of the signal peak, for all the considered decays listed in Table 3.2. These studies are described in Chapter 4.

3.3. Selection

Candidates in this analysis have to pass several subsequent sets of selection requirements, each of them being tighter than the previous one. The procedure starts in the online system, so-called trigger, where relevant signatures of decays are searched. The full reconstruction of candidates is performed. Data are stored after passing requirement of the loose kinematic preselection. Then, in order to obtain the best purity of samples, the dedicated offline selection is applied. Fig. 3.4 symbolically shows the selection steps. The detailed description of the kinematic variables used in the selection are collected in App. A. The trigger and preselection requirements follow usual LHCb requirements and are similar as for other measurements of these modes, for example [21, 40]. The offline selection has been re-optimised since the previous, unpublished studies.

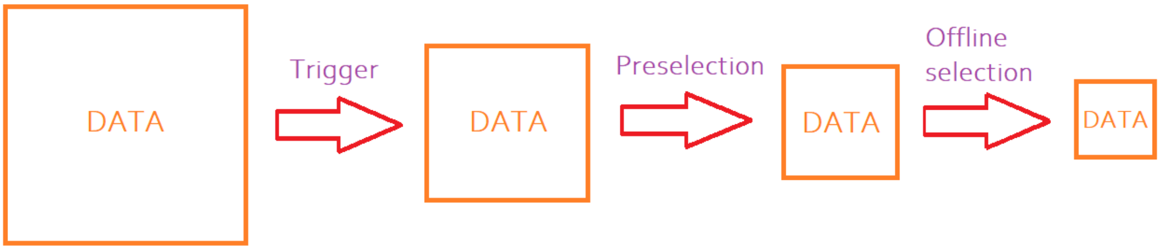

Figure 3.4: The diagram of dataflow with respect to the cuts applied in the analysis. The data set is symbolically drawn as the big orange square with every consecutive cut shown as squares with smaller area, corresponding to less and less events. First the trigger selection takes place, then the preselection and in the end the offline selection.

3.3.1. Trigger

The trigger selection consists of several steps executed in the online system. The first step is hardware (`L0`) which is followed by two software stages (`HLT1` and `HLT2`) [41]. For the first level, Level-0 (`L0`), the data frequency lowers from 40 MHz to 1MHz, so that the detector may read out the incoming data [42]. This trigger is designed to find the general signatures of the decays of interest with unprecedented speed. The `L0` decisions are applied to the candidate based on information from the calorimeters and muon chambers.

Next, the data flow encounters the High Level Trigger (HLT), where the basic track reconstruction takes place. Two levels of HLT are called `HLT1` and `HLT2`. The `HLT1` trigger performs a partial reconstruction of the candidates following the inclusive requirements. In case of the `HLT2` trigger, it contains both inclusive and exclusive algorithms, however the data analysed in this dissertation are using only the inclusive selection. `HLT2` is in main part dedicated to inclusive topological trigger lines, based on multivariate algorithms, that reconstruct all b-hadron decays with charged particles in the final state. These triggers select a displaced two-, three- or four-body vertex. More detailed descriptions are given in [43] and [44] for Run1 and Run2, respectively.

3.3.2. The preselection

The candidates which pass the trigger system are further processed and become the subject of the kinematic selection. At this stage the final state particles are combined and form the charm hadron either D_s^- or $\bar{\Lambda}_c^-$. Next, the charm hadron is combined with the companion particle so that the beauty candidates (either B_s^0 or Λ_b^0) are reconstructed. In order to improve the invariant mass resolution, the kinematic fit [45] is executed with several constraints. First, the beauty candidate is constrained to originate from its associated proton-proton interaction, and secondly the charm hadron (D_s^- or $\bar{\Lambda}_c^-$) mass is fixed to the world average [38]. In addition, a very loose kinematic selection is applied. Figure 3.5 shows the invariant mass distribution of the beauty candidate after passing the preselection. The distributions are given separately for the Run1 (dark colour) and Run2 (light colour) data sets, showing also their relative statistic. In all cases the samples are heavily contaminated with a large fraction of the combinatorial background represented as the exponential distribution.

3.3.3. Offline selection

In order to further improve signal to background ratio in the samples, several steps of the offline selection are distinguished:

- the kinematic selection;
- the PID selection;
- specific background vetoes.

The kinematic selection comprises both rectangular and multivariate requirements as summarised in Tab. B.1 in App. B. For the measurement of the branching fraction the precise estimation of the efficiency selection is needed. In the LHCb experiment

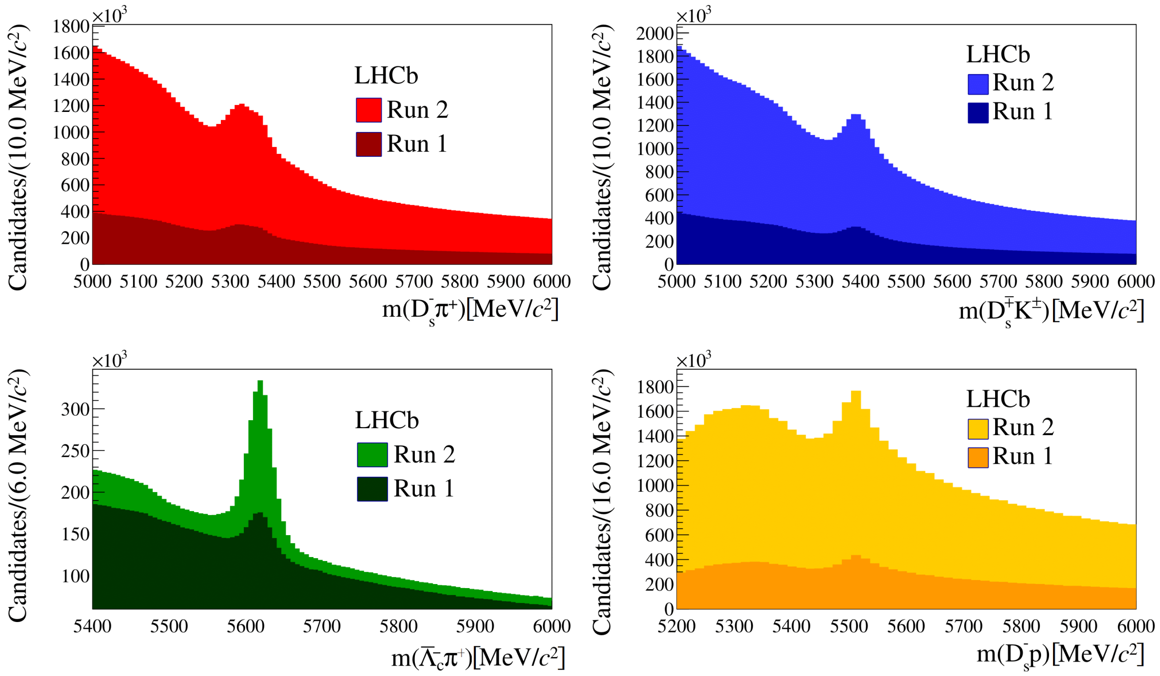

Figure 3.5: The invariant mass distribution for decays studied in this thesis after the preselection. The light colour corresponds to the Run2 sample, while the dark colour indicates Run 1 data set. From the top left to bottom right, for the red, blue, green and yellow colours, the distributions show: $m(D_s^-\pi^+)$, $m(D_s^\mp K^\pm)$, $m(\bar{\Lambda}_c^-\pi^+)$ and $m(D_s^-p)$ invariant masses.

the particle identification performance is obtained from the calibration samples of $D^{*\pm}$ or $\bar{\Lambda}_c^-$ decays [46]. Both, efficiency and misidentification rates, depend on kinematic properties [47] as shown in Fig. 3.6. Therefore, in order to obtain the sensible estimation of these quantities a tight kinematic selection on the final state particles is applied, these are: number of tracks in the event, pseudorapidity η, momentum p and transverse momentum p_T requirements. In addition, a true value for the RICH information is needed as it indicates that the particle identification information is provided.

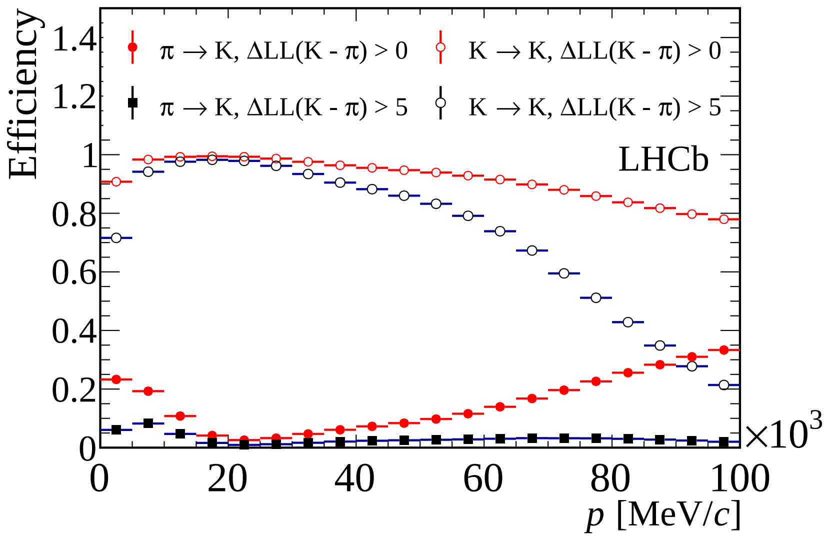

Figure 3.6: The efficiency of the PID performance as the function of the momentum. Taken from Ref. [44]

After the preselection, the combinatorial background is a prime source of sample contamination. To minimise this particular contribution, a multivariate analysis based on the Boosted Decision Tree [48] is performed. More detailed information about this classifier can be found in [49].

In order to separate charmless decay contributions, the charm candidate (either D_s^- or $\bar{\Lambda}_c^-$) needs to satisfy several conditions such as minimal required lifetime, minimal flight distance (FD) (for more details see App. A). In addition, to reduce any contributions from misidentified charm decays a tight charm invariant mass window is applied.

To minimize difference among decays, the same kinematic selection is used for all modes, as shown in Tab. B.1 in App. B. The only difference is the range for the charm and beauty invariant masses, which is a consequence of different particle composition.

The particle identification criteria for the final state particles are defined in Tab. B.2 (App. B). Their role is to select the final state particle under its own hypothesis. To illustrate importance of these requirements the D_s^- invariant mass, $m(h^-h^+h^\pm)$, from the $B_s^0 \to D_s^-\pi^+$ decays is shown in Fig. 3.7 for candidates passing or failing these requirements. The background contamination in the upper side of invariant mass occurs due to misidentification of final state particles and is sufficiently suppressed by applied PID criteria.

In order to describe the hypotheses that might distort the distributions considered in analysis, the specific background vetoes are applied, as written in Table B.3 (App. B)

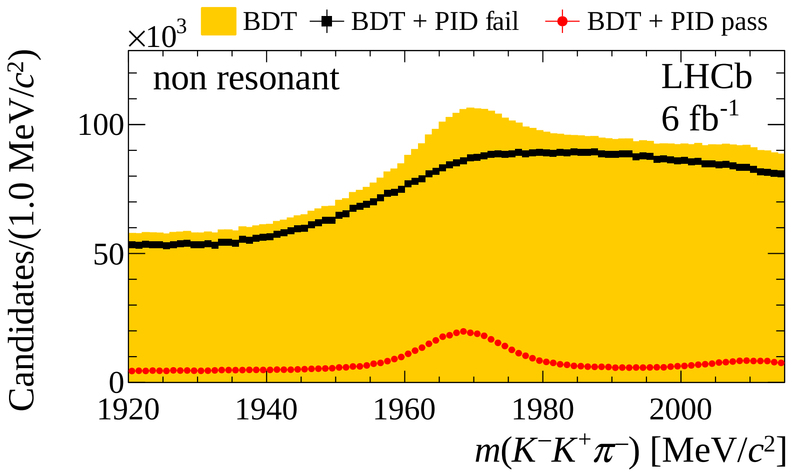

Figure 3.7: The D_s^- invariant mass, $m(h^-h^+h^{\pm})$, distribution from the $B_s^0 \to D_s^-\pi^+$ candidates after the BDT selection (orange) and for candidates passing (red circles) or failing (black squares) the PID selection on the D_s^- children. Taken from Ref. [50].

following the LHCb publication [40]. In the data samples the decays of D_s^-, D^- and $\overline{\Lambda}_c^-$ are a source of background contamination for each other, which occurs due to a wrong identification of the final state particle. Figure 3.8 illustrates this process. In case of decays with D_s^- meson, the kaon with the same charge as the D_s^- meson, namely K^-, is a subject of a single misidentification to either a pion π^- or an antiproton $\bar{p}$ forming D^- or $\overline{\Lambda}_c^-$ hadrons, respectively. Due to a single misdentification these background contributions fall directly under a signal peak, and thus are dangerous for the unbiased yield estimation. In addition, the contribution from the D^0 decays such as $D^0 \to K^+K^-$ is also vetoed in order to prevent *e.g.* $B^0 \to D^{*-}\pi^+$, $D^0 \to K^+K^-$ contamination. Finally, the $\mu^- \leftrightarrow \pi^-$ misidentification might result in contribution from the $B_s^0 \to J/\psi\phi$ decays, which is vetoed with usage of the decided PID variable.

The beauty hadron invariant mass distributions after the full selection are shown in Fig. 3.9. To see the impact of applied requirement the distributions should be compared to the one presented in Fig. 3.5. The combinatorial and misidentified backgrounds are significantly reduced, in all cases the signal peak is easily noticeable.

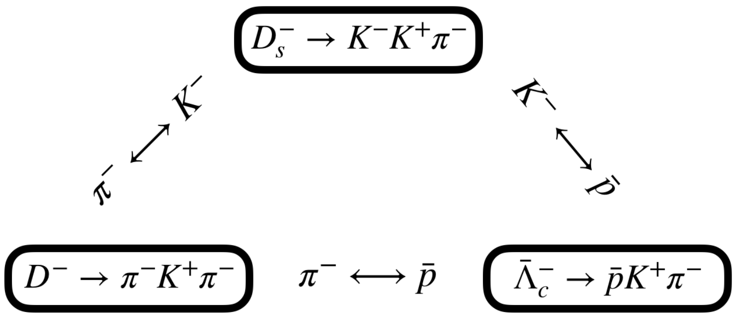

Figure 3.8: The mechanism of misidentification among D_s^-, D^- and $\overline{\Lambda}_c^-$ decays.

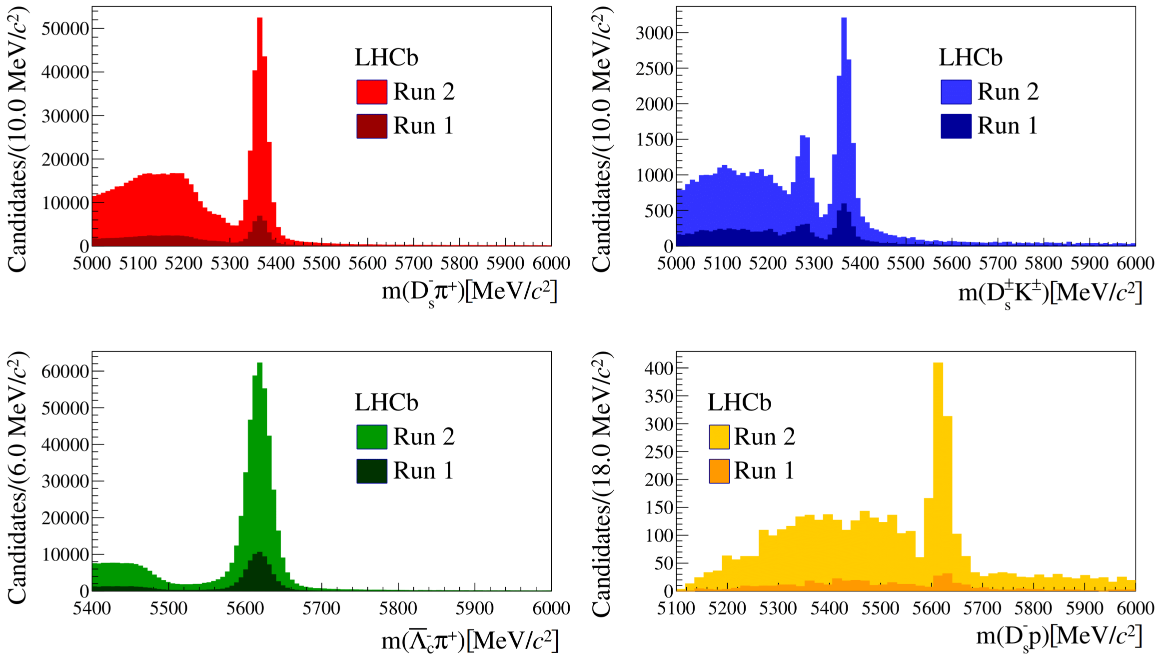

Figure 3.9: The beauty hadron invariant mass distribution for decays studied in this thesis after the full selection. The light colour corresponds to the Run2 sample, while the dark colour indicates Run 1 data set. From the top left to bottom right, for the red, blue, green and yellow colours, the distributions show: $m(D_s^-\pi^+)$, $m(D_s^{\mp}K^{\pm})$, $m(\bar{\Lambda}_c^{\,-}\pi^+)$ and $m(D_s^-p)$ invariant masses.

3.4. Selection efficiencies

For the estimation of the branching ratio of $\Lambda_b^0 \to D_s^- p$ to $\bar{\Lambda}_b^0 \to \bar{\Lambda}_c^- \pi^+$, as given by the Eq. (1.4), the efficiencies $\epsilon(\Lambda_b^0 \to (D_s^- \to K^-K^+\pi^-)p$ and $\epsilon(\bar{\Lambda}_b^0 \to (\bar{\Lambda}_c^- \to \bar{p}K^+\pi^-)\pi^+)$ for all mentioned cuts should be calculated. According to Ref. [51], PID variables in simulation give only the approximate values and need to be obtained using dedicated calibration samples. Thus they can not be directly used for the efficiency calculations. For the sake of this thesis, the calculations are not done, but will be for the future analysis.

Chapter 4

Fit strategy

For the invariant mass distributions of $\Lambda_b^0 \to D_s^- p$ and $\overline{\Lambda}_b^0 \to \overline{\Lambda}_c^- \pi^+$ many separate components that may lay in the same mass range need to be distinguished. In order to properly use this information, for modelling both signal and background contributions official LHCb simulation samples are used.

Due to the known data to simulation discrepancy for the kinematic variables, all samples are corrected based on the observed difference for the $B^0 \to D^- \pi^+$ decay as obtained for the LHCb publication [50]. In addition, the particle identification variables are corrected with usage of the PIDCalib LHCb software package [51]. After these adjustments the discrepancy between data and simulation is reduced. If not stated otherwise, the shapes of specific background components are obtained from so-called templates, predefined parametrisations that have no free parameter other than the normalisation and are mostly obtained using the kernel method [52] implemented in the `RooKeysPdf` class in the RooFit framework [53].

The analysis uses the `PhysFit/B2DXFitters` fitting package, which is a part of the `Urania` LHCb software. In the package the background models are set based on the experience from other measurements [21, 50] and previous studies of these modes [37]. All fits presented in this Chapter are unbinned extended maximum likelihood fits with combined magnet polarities and years of data taking in given run. The value of χ^2/ndf shown together with Figures depends on the number of bins and serves only as the indication for stability, but they are not used during the fitting procedure.

The scope of this thesis included:

1. updating all configuration files needed for the fits presented in this Chapter (both in the nominal invariant mass range and beauty hadron invariant mass sideband) after re-optimisation of offline selection collected in Sec. 3.3.3;

2. preparation of the offline selected data and simulation samples in so-called `RooWorkspaces` required by the `PhysFit/B2DXFitters` fitting package, together with obtaining all shapes for specific backgrounds;

3. understanding the nature of background contribution i.e. how and why they contribute to the given sample;

4. establishing the combinatorial background parametrisation from the beauty hadron invariant mass sideband;

5. performing preliminary fits to the control, normalisation and signal samples.

The work presented in this thesis is done in the collaboration with NIKHEF group, where the collaborators provided the signal parametrisations as well as yields estimation for those background contributions which are less than 1% of signal in given sample.

4.1. The invariant mass fit to the $B_s^0 \to D_s^- \pi^+$ sample

In order to estimate the contribution from the $D_s^- \pi^+$-like decays in the $B_s^0 \to D_s^\mp K^\pm$ and $\Lambda_b^0 \to D_s^- p$ data samples, an invariant mass fit to the $B_s^0 \to D_s^- \pi^+$ sample under its own hypothesis is used. The fit strategy closely follows the one from the LHCb publications [49] and [50]. However, due to the different selection criteria as well as including all available Run1 and Run2 data sets, the fit is performed for the purpose of this particular analysis.

The $B_s^0 \to D_s^- \pi^+$ signal description is directly taken from Ref. [50] where the fits to the simulation samples were performed.

The specific background contributions to the fit are described in Tab. 4.1 together with the description how they contribute to the sample. Three different sources of background can be distinguished: the decays with the same final state as the signal ($B^0 \to D_s^- \pi^+$), the misidentified backgrounds ($B^0 \to D^- \pi^+$, $\overline{\Lambda}_b^0 \to \overline{\Lambda}_c^- \pi^+$, $B_s^0 \to D_s^\mp K^\pm$) and the partially reconstructed backgrounds which occur due to missing particles in the final state ($B_s^0 \to D_s^{*-} \pi^+$, $B_s^0 \to D_s^- \rho^+$, $B_s^0 \to D_s^{*-} \rho^+$). Together with the signal, $B_s^0 \to D_s^- \pi^+$, the last group consist of so-called $D_s^- \pi^+$-like components, and their yield is a subject of study.

Table 4.1: Specific backgrounds considered in the $B_s^0 \to D_s^- \pi^+$ sample.

Decay chain	How it contributes
$B^0 \to D_s^- \pi^+$	Same final state
$B_s^0 \to D_s^\mp K^\pm$	$K^+ \to \pi^+$ (companion)
$B^0 \to D^- \pi^+ \to (K^+ \pi^- \pi^-) \pi^+$	$\pi^- \to K^-$ (D^-)
$\overline{\Lambda_b^0} \to \overline{\Lambda}_c^- \pi^+ \to (\overline{p} K^+ \pi^-) \pi^+$	$\overline{p} \to K^-$ $(\overline{\Lambda}_c^-)$
$B_s^0 \to D_s^{*-} \pi^+ \to D_s^- \gamma \pi^+$	Missing photon γ
$B_s^0 \to D_s^- \rho^+ \to D_s^- \pi^+ \pi^0.$	Missing π^0
$B_s^0 \to D_s^{*-} \rho^+ \to D_s^- \gamma \pi^+ \pi^0$	Missing γ and π^0

The functional form of the combinatorial background is taken from the $D_s^- \pi^+$ invariant mass $m(D_s^- \pi^+)$ sideband defined as $m(D_s^- \pi^+) \in [5600, 6800]\,\mathrm{MeV}/c^2$. Two parametrisations are considered: a single and double exponential. An exponential function $\mathcal{C}(m|c_i)$ with a slope c_i is defined as the Eq. 4.1 reads:

$$\mathcal{C}(m|c_i) \equiv e(m|c_i) = e^{-c_i \cdot m}, \tag{4.1}$$

while a double exponential definition, for slopes c_1, c_2 and fraction between two components f, is shown in Eq. 4.2:

$$\begin{aligned} \mathcal{C}(m|c_1, c_2, f) = \\ f \cdot e(m|c_1) + (1-f) \cdot e(m|c_2). \end{aligned} \tag{4.2}$$

The fits to the data sideband are presented in Fig. 4.1 separately for the Run1 and Run2 data samples. The numerical results are listed in Tab. 4.2. In both cases, the better χ^2/ndf is obtained for the double exponential function and thus this parametrisation is used in the nominal data fit.

For the double exponential approach, fit returns one slope (c_1) proportional to 10^{-3} and second one order of magnitude bigger ($c_2 \sim 10^{-2}$). In the nominal data fit, in order to cover for any difference between shapes in the sideband and in the nominal fit region of $m(D_s^-\pi^+) \in [5000, 6000]\,\text{MeV}/c^2$, the smaller slope ($c_1$) is fixed to the value found in the sideband, whereas the second slope (c_2) and the fraction between two components f are left free. As the fitting procedure does not have access to data in the low mass region, it is not expected that the values in the nominal fit should follow the one obtained in the sideband. However, the function form can be assumed to be the same. Similar conclusion has been made in the other LHCb publication of these modes [50].

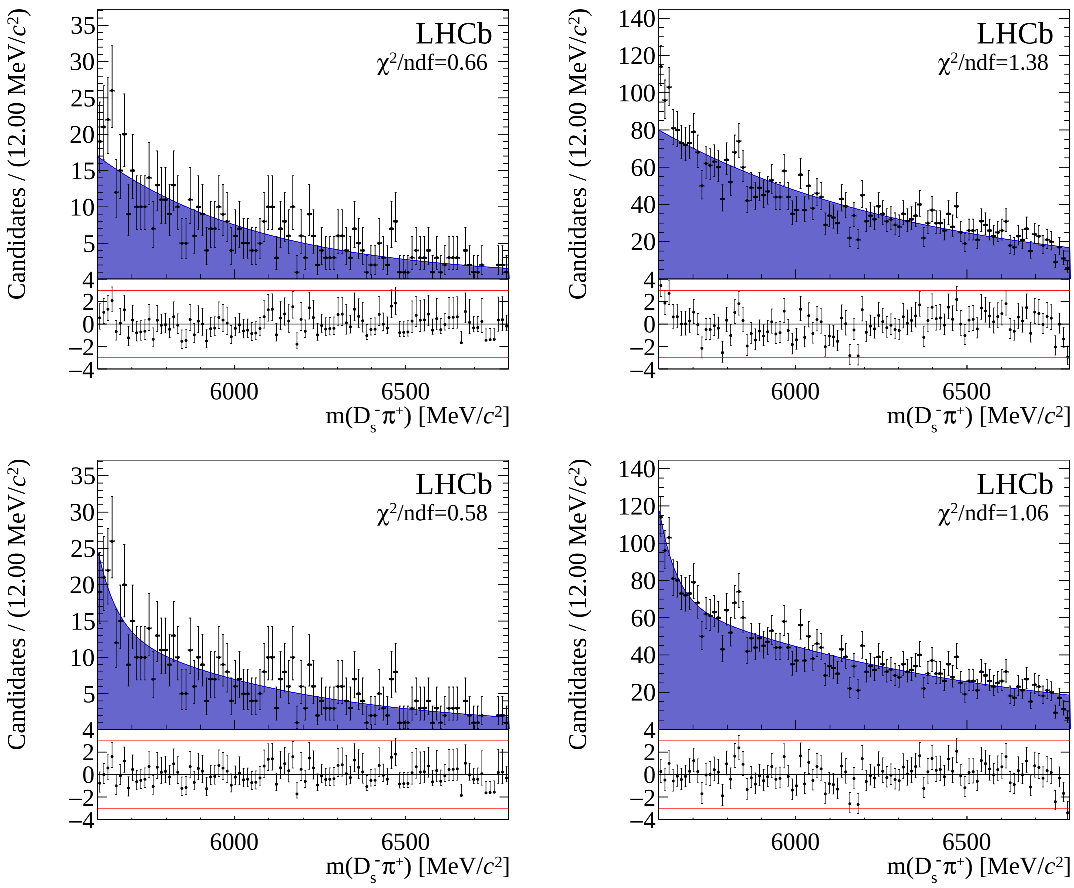

Figure 4.1: The invariant mass $m(D_s^-\pi^+)$ distribution for the B_s^0 sideband $m(D_s^-\pi^+) \in [5600, 6800]\,\text{MeV}/c^2$. In this region only the combinatorial background is considered. The results are split for the data taking period Run1 (left) and Run2 (right) as well as two parametrisations: a single exponential (top) and a double exponential (bottom). The lower part of each figure shows the residual of the data points with respect to the fit, normalised to the uncertainty of the data points.

Table 4.2: Parameters of the single (c) and double exponential (c_1,c_2,f) functions describing the combinatorial background invariant mass $m(D_s^- \pi^+)$ in the $B_s^0 \to D_s^- \pi^+$ sample, obtained from a fit to the sideband: $m(D_s^- \pi^+) \in [5600, 6800]\,\mathrm{MeV}/c^2$. Right column describes the behaviour in the nominal fit to data. The corresponding results of the fit are shown in Fig. 4.1.

Parameter	Run1	Run2	Behaviour in data fit
$c_1 \times 10^{-3}\ [\mathrm{MeV}/c^2]^{-1}$	-1.77 $\pm$ 0.19	-1.119 $\pm$ 0.072	fixed
$c_2 \times 10^{-2}\ [\mathrm{MeV}/c^2]^{-1}$	-1.82 $\pm$ 0.87	-1.99 $\pm$ 0.72	free
f	0.923 $\pm$ 0.039	0.950 $\pm$ 0.016	free
$c \times 10^{-3}\ [\mathrm{MeV}/c^2]^{-1}$	-2.05 $\pm$ 0.13	-1.313 $\pm$ 0.048	free

In order to stabilise fitting procedure some background components are merged in groups and other are fixed. The yields which are below <1% of the signal component ($B_s^0 \to D_s^\mp K^\pm$, $B^0 \to D^- \pi^+$, $\Lambda_b^0 \to \bar{\Lambda}_c^- \pi^+$) are fixed from the branching ratios and efficiency predictions. The partially reconstructed backgrounds ($B_s^0 \to D_s^{*-} \pi^+$, $B_s^0 \to D_s^- \rho^+$, $B_s^0 \to D_s^{*-} \rho^+$) are merged into one component $n_{partReco}$ following recursive procedure for $n_{X\to Y}$ being the yield of $X \to Y$ decay and relative ratios denoted f_i for $i+1$ decays merged:

$$\begin{aligned} n_{partReco} = & f_1 \times n_{B_s^0 \to D_s^{*-} \pi^+} \\ & + (1 - f_1) \times f_2 \times n_{B_s^0 \to D_s^- \rho^+} \\ & + (1 - f_1) \times (1 - f_2) \times n_{B_s^0 \to D_s^{*-} \rho^+} \end{aligned} \tag{4.3}$$

For the analysis, the values of $n_{partReco}$, f_1 and f_2 are of importance, as the partially reconstructed backgrounds. These decays together with the signal $B_s^0 \to D_s^- \pi^+$ channel are a major background to other modes such as the $B_s^0 \to D_s^\mp K^\pm$ and eventually $\Lambda_b^0 \to D_s^- p$ samples. Their yield corrected by the efficiency ratio of the relevant PID requirements provide data-driven information about expected contribution in other samples. The partially reconstructed backgrounds enter the signal region $m(D_s^- \pi^+) \in [m_{B_s^0} - 50.00, m_{B_s^0} + 50.00]\,\mathrm{MeV}/c^2$, where $m_{B_s^0}$ is the B_s^0 meson mass (see Table 3.4). These backgrounds behaviour in correspondence to each other and the $B_s^0 \to D_s^- \pi^+$ decay channel, e.g. the yields ratios, is a great indicator whether the nominal mass fit is stable. The fit for $B_s^0 \to D_s^- \pi^+$ Run1 and Run2 is shown in Fig. 4.2. Together with $B_s^0 \to D_s^- \pi^+$ yield, denoted $n_{B_s^0 \to D_s^- \pi^+}$, the $n_{partReco}$ and ratios values after the nominal mass fit are listed in Table 4.3.

One of the most prominent behaviours the Table suggests is that the f_2 ratio tends to take the values close to unity, for both Run1 and Run2 data sets, with higher uncertainty for Run2. The difference in the orders of values of uncertainties is most likely induced by the fact that f_2 ratio introduced a new degree of freedom, distorting the fitting procedure conducted on a high statistics Run2 data set. Looking at Eq. (4.3) and results for Run1 data set, it is a suggestion that the background of $B_s^0 \to D_s^{*-} \rho^+$ in $B_s^0 \to D_s^- \pi^+$ sample is negligibly small and possibly needs a dedicated modelling for the future analysis.

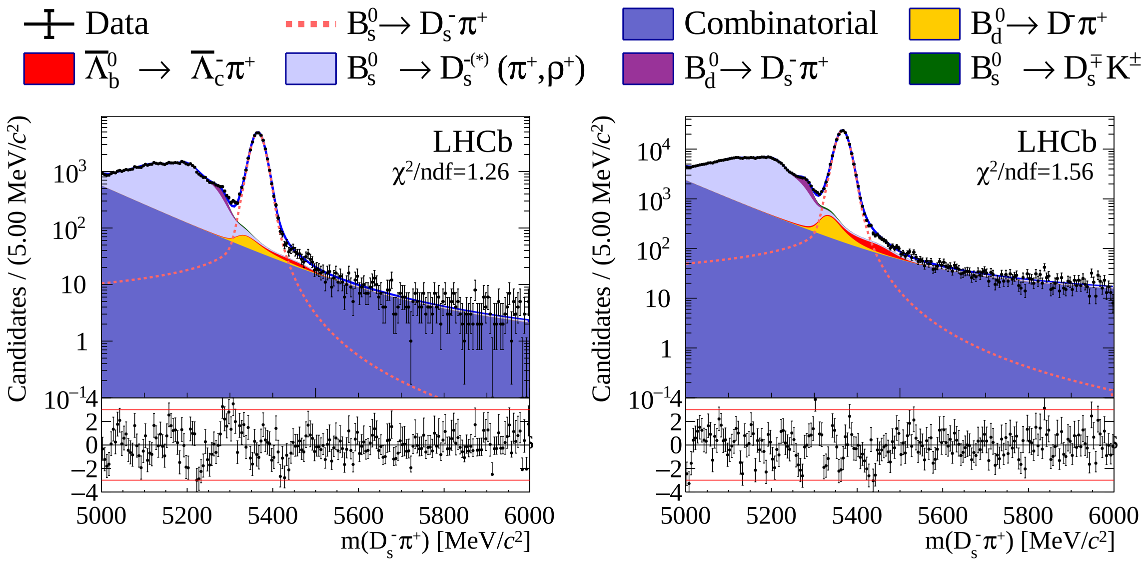

Figure 4.2: Nominal mass fit for $B_s^0 \to D_s^- \pi^+$ Run1 (left) and Run2 (right) in logarithmic scale with shared legend (top). The lower part of each figure shows the residual of the data points with respect to the fit, normalised to the uncertainty of the data points.

Table 4.3: Parameters describing the nominal invariant mass $m(D_s^- \pi^+)$ fit in the $B_s^0 \to D_s^- \pi^+$ sample in total range: $m(D_s^- \pi^+) \in [5000, 6000]$ MeV/c^2. The signal range is defined ± 50 MeV/c^2 around nominal B_s^0 mass (see Table 3.4). The parameters $n_{partReco}$, f_1 and f_2 are the partially reconstructed backgrounds yields and their relative ratios, as given by Eq. (4.3), while $n_{B_s^0 \to D_s^- \pi^+}$ is the $B_s^0 \to D_s^- \pi^+$ yield. The yields are given for the total range. The corresponding results of the fit are shown in Fig. 4.2. Columns on the bottom describe the fit performance for $B_s^0 \to D_s^- \pi^+$ signal S and its total background B.

Parameters	Run1	Run2
$n_{B_s^0 \to D_s^- \pi^+}$	39040 ± 210	184100 ± 420
$n_{partReco}$	49270 ± 630	249600 ± 4400
f_1	0.652 ± 0.014	0.579 ± 0.013
f_2	1.000 ± 0.011	1.00 ± 0.64

Period	S/B		$S/\sqrt{S+B}$	
	Signal range	Total range	Signal range	Total range
Run1	27.29	0.59	189.92	120.59
Run2	23.77	0.57	411.60	258.88

4.2. The invariant mass fit to the $B_s^0 \to D_s^{\mp} K^{\pm}$ sample

To obtain the contribution from the $D_s^{\mp} K^{\pm}$-like decays in the $\Lambda_b^0 \to D_s^- p$ data samples, an invariant mass fit to the $B_s^0 \to D_s^{\mp} K^{\pm}$ sample under its own hypothesis is used. The fit strategy closely follows the one from the LHCb publication [54]. The $B_s^0 \to D_s^{\mp} K^{\pm}$ signal description is directly taken from Ref. [55] where the fits to the simulation samples were performed. The fit is performed for the purpose of this particular analysis due to different selection criteria as well as including all available Run1 and Run2 data sets.

The specific background contributions to the fit are described in Tab. 4.4 together with the description of how they contribute to the sample. Unlike the case of $B_s^0 \to D_s^- \pi^+$ decay, four different sources of background for $B_s^0 \to D_s^{\mp} K^{\pm}$ signal can be distinguished: the decays with the same final state as the signal ($B^0 \to D_s^- K^+$), the partially reconstructed backgrounds which occur due to missing particles in the final state ($B_s^0 \to D_s^{*\mp} K^{\pm}$, $B_s^0 \to D_s^{\mp} K^{*\pm}$, $B_s^0 \to D_s^{*\mp} K^{*\pm}$), the misidentified backgrounds ($B_s^0 \to D_s^- \pi^+$, $\Lambda_b^0 \to D_s^- p$) and the backgrounds that are both partially reconstructed and misidentified ($B_s^0 \to D_s^{*-} \pi^+$, $B_s^0 \to D_s^- \rho^+$, $B_s^0 \to D_s^{*-} \rho^+$, $\Lambda_b^0 \to D_s^{*-} p$). Due to the tight PID requirement on the companion track the last group of backgrounds is sufficiently suppressed. For the purpose of this study, the contributions from the backgrounds which are expected to be less than 1% of signal yield [55], namely the $B^0 \to D^- \pi^+$ and $\overline{\Lambda}_b^0 \to \overline{\Lambda}_c^- \pi^+$ decays, are neglected.

Two groups mentioned first: the decays with the same final state as the signal and the partially reconstructed backgrounds together with $B_s^0 \to D_s^{\mp} K^{\pm}$ signal can be grouped into the $D_s^{\mp} K^{\pm}$-like decays, that concern this part of the analysis and are the background contributions to the $\Lambda_b^0 \to D_s^- p$ sample.

Table 4.4: Specific backgrounds considered in the $B_s^0 \to D_s^{\mp} K^{\pm}$ sample.

Decay chain	How it contributes
$B^0 \to D_s^- K^+$	Same final state
$B_s^0 \to D_s^- \pi^+$	$\pi^+ \to K^+$ (companion)
$\Lambda_b^0 \to D_s^- p$	$p \to K^+$ (companion)
$B_s^0 \to D_s^{*\mp} K^{\pm} \to D_s^{\mp} \gamma K^{\pm}$	Missing photon γ
$B_s^0 \to D_s^{\mp} K^{*\pm} \to D_s^{\mp} K^{\pm} \pi^0$	Missing π^0
$B_s^0 \to D_s^{*\mp} K^{*\pm} \to D_s^{\mp} \gamma K^{\pm} \pi^0$	Missing photons γ and π^0
$B_s^0 \to D_s^{*-} \pi^+ \to D_s^- \gamma \pi^+$	$\pi^+ \to K^+$ (companion), missing photon γ
$B_s^0 \to D_s^- \rho^+ \to D_s^- \pi^+ \pi^0$	$\pi^+ \to K^+$ (companion), missing π^0,
$B_s^0 \to D_s^{*-} \rho^+ \to D_s^- \gamma \pi^+ \pi^0$	$\pi^+ \to K^+$ (companion), missing π^0 and γ
$\Lambda_b^0 \to D_s^{*-} p \to D_s^- \gamma p$	$p \to K^+$ (companion), missing π^0

The functional form of the combinatorial background is taken from the $D_s^{\mp} K^{\pm}$ invariant mass $m(D_s^{\mp} K^{\pm})$ sideband defined as $m(D_s^{\mp} K^{\pm}) \in [5600, 6800]\,\text{MeV}/c^2$. Two parametrisations are considered: a single and double exponential, analogous to $B_s^0 \to D_s^- \pi^+$ considerations in Eq. (4.1) and (4.2).

The fits to the data sideband are presented in Fig. 4.3 separately for the Run1 and Run2 data samples. The numerical results are listed in Tab. 4.5. Although the better χ^2/ndf was obtained for the double exponential shape (bottom row), the single exponential shape was chosen, because of the possible instability of the shape, as it can be seen at the bottom right plot, double exponential and Run2, where for the lower range of invariant mass the slope significantly jumps to high numbers of events. In both cases the fraction f returns a value very close to 1. This results in the high uncertainty of obtained c_2 parameter, proving that the single exponential is sufficient parametrisation. This is in agreement with the conclusion made in the previous LHCb analysis of these modes [21].

For the nominal data fit, in order to cover for the shape of the sideband in the nominal fit region of $m(D_s^{\mp}K^{\pm}) \in [5000, 6000]\,\text{MeV}/c^2$, the slope $c \sim 10^{-3}$ is fixed. The values of parameters obtained in the combinatorial background mass fit are written in Table 4.5.

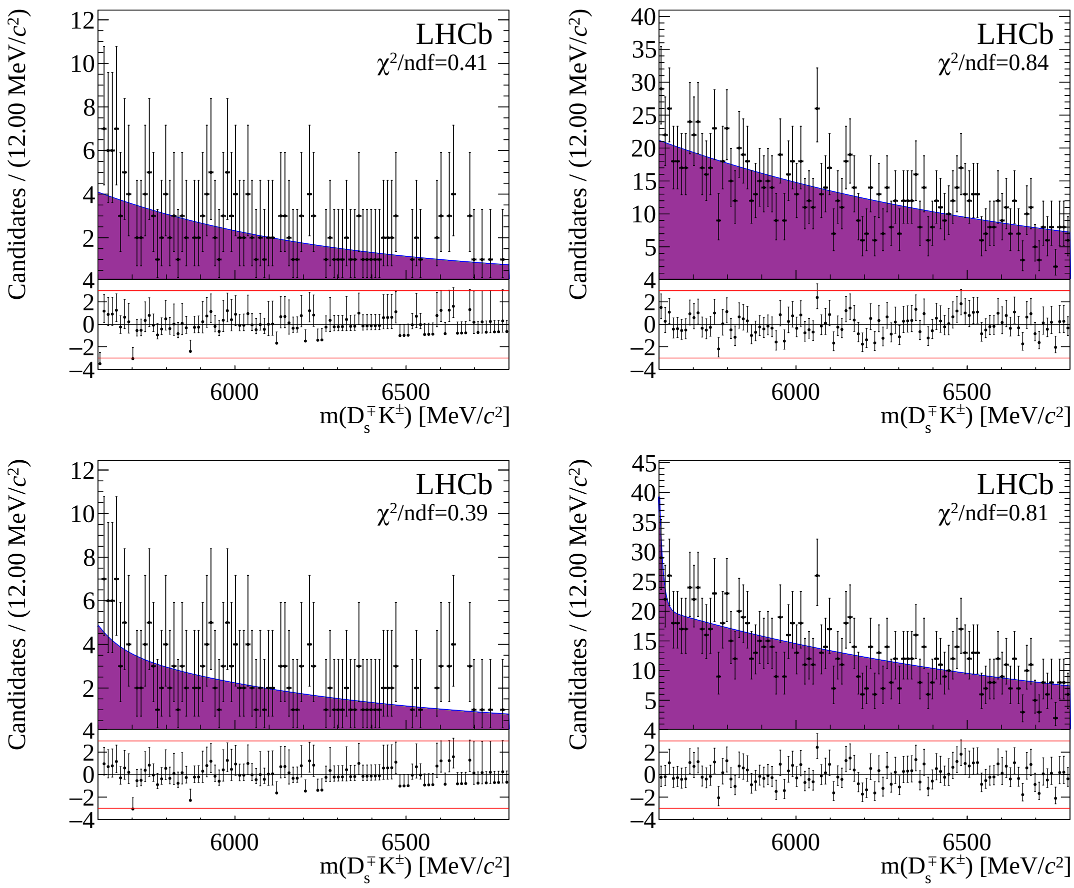

Figure 4.3: The invariant mass $m(D_s^{\mp}K^{\pm})$ distribution for the B_s^0 sideband $m(D_s^{\mp}K^{\pm}) \in [5600, 6800]\,\text{MeV}/c^2$. In this region only the combinatorial background is considered. The results are split for the data taking period Run1 (left) and Run2 (right) as well as two parametrisations: a single exponential (top) and a double exponential (bottom). The lower part of each figure shows the residual of the data points with respect to the fit, normalised to the uncertainty of the data points.

In order to stabilise fitting procedure some background components are merged in groups in the same manner as done in Ref. [55]. The first group includes backgrounds

Table 4.5: Parameters of the single (c) and double exponential (c_1,c_2,f) functions describing the combinatorial background invariant mass $m(D_s^{\mp}K^{\pm})$ in the $B_s^0 \to D_s^{\mp}K^{\pm}$ sample, obtained from a fit to the sideband: $m(D_s^{\mp}K^{\pm}) \in [5600, 6800]\,\mathrm{MeV}/c^2$. Right column describes the behaviour in the nominal fit to data. The corresponding results of the fit are shown in Fig. 4.3.

Parameter	Run1	Run2	Behaviour in data fit
$c_1 \times 10^{-4}$ $[\mathrm{MeV}/c^2]^{-1}$	-13.1 ± 3.0	-8.50 ± 0.87	free
$c_2 \times 10^{-3}$ $[\mathrm{MeV}/c^2]^{-1}$	-14 ± 15	-101 ± 70	free
f	0.966 ± 0.058	0.9878 ± 0.0067	free
$c \times 10^{-3}$ $[\mathrm{MeV}/c^2]^{-1}$	-1.43 ± 0.22	-0.903 ± 0.083	fixed

where a kaon K^+ is properly identified among the final state particles ($B^0 \to D_s^- K^+$, $B_s^0 \to D_s^{*\mp}K^{\pm}$, $B_s^0 \to D_s^{\mp}K^{*\pm}$, $B_s^0 \to D_s^{*\mp}K^{*\pm}$) are merged into one component $n_{B_{(s)}^0 \to D_s^{(*)\mp} K^{(*)\pm}}$ following recursive procedure, for $n_{X\to Y}$ being the yield of $X \to Y$ decay and relative ratios denoted f_{1i} for $i+1$ decays merged, as written in Eq. (4.4):

$$\begin{aligned} n_{B_{(s)}^0 \to D_s^{(*)\mp} K^{(*)\pm}} =& f_{11} \times n_{B^0 \to D_s^- K^+} \\ &+ (1-f_{11}) \times f_{12} \times n_{B_s^0 \to D_s^{*\mp} K^{\pm}} \\ &+ (1-f_{11}) \times (1-f_{12}) \times f_{13} \times n_{B_s^0 \to D_s^{\mp} K^{*\pm}} \\ &+ (1-f_{11}) \times (1-f_{12}) \times (1-f_{13}) \times n_{B_s^0 \to D_s^{*\mp} K^{*\pm}}. \end{aligned} \tag{4.4}$$

Similar recursive procedure is applied for the second group of distinguished backgrounds for $B_s^0 \to D_s^{\mp}K^{\pm}$ which comprise the decays where the pion π^+ is mistaken for a companion kaon K^+ ($B_s^0 \to D_s^- \pi^+$, $B_s^0 \to D_s^{*-}\pi^+$, $B_s^0 \to D_s^- \rho^+$, $B_s^0 \to D_s^{*-}\rho^+$). Thus the Eq. (4.5) for a component $n_{B_s^0 \to D_s^{(*)-}(\pi^+,\, \rho^+)}$ is given with relative ratios denoted f_{2i} for $i+1$ decays merged:

$$\begin{aligned} n_{B_s^0 \to D_s^{(*)-}(\pi^+,\, \rho^+)} =& f_{21} \times n_{B_s^0 \to D_s^- \pi^+} \\ &+ (1-f_{21}) \times f_{22} \times n_{B_s^0 \to D_s^{*-} \pi^+} \\ &+ (1-f_{21}) \times (1-f_{22}) \times f_{23} \times n_{B_s^0 \to D_s^- \rho^+} \\ &+ (1-f_{21}) \times (1-f_{22}) \times (1-f_{23}) \times n_{B_s^0 \to D_s^{*-} \rho^+}. \end{aligned} \tag{4.5}$$

The third group of decays are the Λ_b^0 decays where the companion proton p is mistaken for a kaon K^+ ($\Lambda_b^0 \to D_s^- p$, $\Lambda_b^0 \to D_s^{*-} p$). The recursive procedure can be applied just as for the following equations, allowing to obtain the component $n_{\Lambda_b^0 \to D_s^{(*)-} p}$ in Eq. (4.6) for relative ratio that is fixed from predictions $f_{31} = 0.75$:

$$\begin{aligned} n_{\Lambda_b^0 \to D_s^{(*)-} p} =& f_{31} \times n_{\Lambda_b^0 \to D_s^- p} \\ &+ (1-f_{31}) \times n_{\Lambda_b^0 \to D_s^{*-} p}. \end{aligned} \tag{4.6}$$

So far, three groups of $B_s^0 \to D_s^{\mp} K^{\pm}$ background have been established for the nominal mass fitting procedure to be stable: with a kaon K^+ properly identified among the final state particles, with a pion π^+ misidentified as a kaon K^+ and with a proton p misidentified as a kaon K^+. For further simplification of decays grouping, two last groups can be merged into the group containing all decays where the final state particle was misidentified as a kaon K^+. All of these contributions are heavily suppressed due to a tight PID requirement on the companion track. Two background groups are merged with relative fraction f_{51}. Thus the component $n_{(B_s^0,\, \Lambda_b^0) \to D_s^{(*)-}(p,\, \pi^+,\, \rho^+)}$ is obtained:

$$\begin{aligned} n_{(B_s^0,\, \Lambda_b^0) \to D_s^{(*)-}(p,\, \pi^+,\, \rho^+)} =& f_{51} \times n_{B_s^0 \to D_s^{(*)-}(\pi^+,\, \rho^+)} \\ &+ (1 - f_{51}) \times n_{\Lambda_b^0 \to D_s^{(*)-} p}. \end{aligned} \tag{4.7}$$

This way, the fitting procedure is stable, as can be seen in Fig. 4.4, where the nominal mass fits for $B_s^0 \to D_s^{\mp} K^{\pm}$ Run1 and Run2 are shown. The dominant source of the background is the partially reconstructed group (shown as light blue). Other specific backgrounds as well as the combinatorial background are sufficiently suppressed. The fit quality is proven by the χ^2/ndf value being 0.84 and 1.19 for Run 1 and Run2, respectively. A small mismatch between the data and model in the region below $m(D_s^{\mp} K^{\pm}) < 5200\ \mathrm{MeV}/c^2$ is a result of low statistic in the simulation sample, and as a consequence large fluctuation of the $B_s^0 \to D_s^{\mp} K^{*\pm}$ shape. In order to improve the quality of the fit, a dedicated parametrisation to these samples should be provided, which is a subject of future studies.

In order to obtain the $D_s^{\mp} K^{\pm}$-like backgrounds in the $\Lambda_b^0 \to D_s^- p$ sample following variables are of interest: the signal $B_s^0 \to D_s^{\mp} K^{\pm}$ yield, the total yield of the partially reconstructed backgrounds $n_{B_{(s)}^0 \to D_s^{(*)\mp} K^{(*)\pm}}$ as well as their relative fractions, f_{11}, f_{12} and f_{13}. These parameters are reported in Tab. 4.6. Together with the information about relative PID efficiency of requirements applied to select the $B_s^0 \to D_s^{\mp} K^{\pm}$ and $\Lambda_b^0 \to D_s^- p$ decays, this study can be used in order to obtain $D_s^{\mp} K^{\pm}$-like backgrounds contribution in the $\Lambda_b^0 \to D_s^- p$ sample.

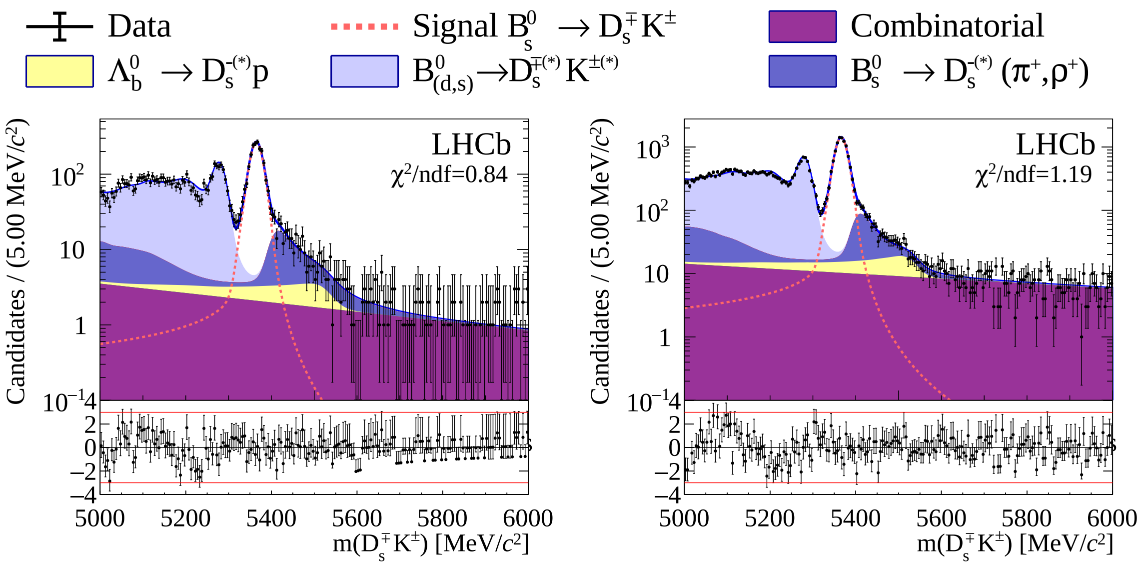

Figure 4.4: Nominal mass fit for $B_s^0 \to D_s^{\mp} K^{\pm}$ Run1 (left) and Run2 (right) in logarithmic scale with shared legend (top). The lower part of each figure shows the residual of the data points with respect to the fit, normalised to the uncertainty of the data points.

Table 4.6: Parameters describing the nominal invariant mass $m(D_s^{\mp} K^{\pm})$ fit in the $B_s^0 \to D_s^{\mp} K^{\pm}$ sample in total range: $m(D_s^{\mp} K^{\pm}) \in [5000, 6000]\,\mathrm{MeV}/c^2$. The signal range is defined $\pm 50\,\mathrm{MeV}/c^2$ around nominal B_s^0 mass (see Table 3.4). The parameters $n_{B_{(s)}^0 \to D_s^{(*)\mp} K^{(*)\pm}}$, f_{11}, f_{12}, f_{13} describe backgrounds yields and relative ratios, as given by Eq. (4.4) while $n_{B_s^0 \to D_s^{\mp} K^{\pm}}$ is the $B_s^0 \to D_s^{\mp} K^{\pm}$ yield. The corresponding results of the fit are shown in Fig. 4.4. Columns on the bottom describe the fit performance for $B_s^0 \to D_s^{\mp} K^{\pm}$ signal S and its total background B.

Parameter	Run1	Run2
$n_{B_s^0 \to D_s^{\mp} K^{\pm}}$	2064 ± 49	10450 ± 110
$n_{B_{(s)}^0 \to D_s^{(*)\mp} K^{(*)\pm}}$	4227 ± 75	21270 ± 160
f_{11}	0.192 ± 0.012	0.1916 ± 0.0046
f_{12}	0.732 ± 0.081	0.702 ± 0.034
f_{13}	0.45 ± 0.21	0.453 ± 0.082

Period	S/B		$S/\sqrt{S+B}$	
	Signal range	Total range	Signal range	Total range
Run1	11.69	0.40	42.69	24.21
Run2	11.57	0.41	96.14	55.06

4.3. The invariant mass fit to the $\overline{\Lambda}_b^0 \to \overline{\Lambda}_c^- \pi^+$ sample

To estimate the branching fraction of $\Lambda_b^0 \to D_s^- p$ decay, its signal yield is normalised with respect to the $\overline{\Lambda}_b^0 \to \overline{\Lambda}_c^- \pi^+$ channel, just as described in Section 3.1, thus the value of the $\overline{\Lambda}_b^0 \to \overline{\Lambda}_c^- \pi^+$ yield is of great importance for the analysis. The invariant mass fit to the $\overline{\Lambda}_b^0 \to \overline{\Lambda}_c^- \pi^+$ sample under its own hypothesis is used. The fit strategy closely follows the one from the LHCb publication [56]. The signal description is taken from the fits to the simulation samples and provided by the collaborators from NIKHEF.

The specific background contributions to the fit are described in Tab. 4.7 together with how they contribute to the sample. For the $\overline{\Lambda}_b^0 \to \overline{\Lambda}_c^- \pi^+$ signal two different sources of background can be distinguished: the partially reconstructed backgrounds which occur due to missing particles in the final state ($\overline{\Lambda}_b^0 \to \overline{\Lambda}_c^- \rho^+$, $\overline{\Lambda}_b^0 \to \overline{\Sigma}_c^- \pi^+$) and the misidentified backgrounds ($\overline{\Lambda}_b^0 \to \overline{\Lambda}_c^- K^+$, $B_s^0 \to D_s^- \pi^+$, $B^0 \to D^- \pi^+$). The yields of the misidentified backgrounds are expected to be about 1% of the signal $\overline{\Lambda}_b^0 \to \overline{\Lambda}_c^- \pi^+$ candidates. Their contributions should be calculated from the measured branching ratios and relative efficiencies. It is a subject of the future studies.

Table 4.7: Specific backgrounds considered in the $\overline{\Lambda}_b^0 \to \overline{\Lambda}_c^- \pi^+$ sample.

Decay chain	How it contributes
$\overline{\Lambda}_b^0 \to \overline{\Lambda}_c^- \rho^+ \to \overline{\Lambda}_c^- \pi^+ \pi^0$	Missing π^0
$\overline{\Lambda}_b^0 \to \overline{\Sigma}_c^- \pi^+ \to \overline{\Lambda}_c^- \pi^0 \pi^+$	Missing π^0
$\overline{\Lambda}_b^0 \to \overline{\Lambda}_c^- K^+$	$K^+ \to \pi^+$ (companion)
$B_s^0 \to D_s^- \pi^+ \to (K^- K^+ \pi^-) \pi^+$	$K^- \to \overline{p}$ (D_s^-)
$B^0 \to D^- \pi^+ \to (\pi^- K^+ \pi^-) \pi^+$	$\pi^- \to \overline{p}$ (D^-)

Similarly to other decays, the combinatorial background parametrisation is verified by studying the $\bar{\Lambda}_b^0$ sideband defined as $m(\bar{\Lambda}_c^- \pi^+) \in [5750, 6800]\,\mathrm{MeV}/c^2$. The values of parameters obtained in the combinatorial background mass fit are written in Table 4.8, while the fits are shown in Fig. 4.5. Better χ^2/ndf is obtained for the double exponential shape (bottom row), as it would be expected. For the nominal mass fit, the smaller slope ($\sim 10^{-4}$) is fixed while the bigger ($\sim 10^{-3}$) slope is left floating. Due to kinematic differences between the sideband and nominal mass fit range, it is not expected that the values obtained in the nominal fit should closely follow the one in the sideband, however a functional form should stay the same.

Table 4.8: Parameters of the single (c) and double exponential (c_1,c_2,f) functions describing the combinatorial background invariant mass $m(\bar{\Lambda}_c^- \pi^+)$ in the $\bar{\Lambda}_b^0 \to \bar{\Lambda}_c^- \pi^+$ sample, obtained from a fit to the sideband: $m(\bar{\Lambda}_c^- \pi^+) \in [5750, 6800]\,\mathrm{MeV}/c^2$. Right column describes the behaviour in the nominal fit to data. The corresponding results of the fit are shown in Fig. 4.5.

Parameter	Run1	Run2	Behaviour in data fit
$c_1 \times 10^{-4}$ $[\mathrm{MeV}/c^2]^{-1}$	-7.5 ± 6.1	-0.5 ± 3.4	fixed
$c_2 \times 10^{-3}$ $[\mathrm{MeV}/c^2]^{-1}$	-9.0 ± 5.3	-6.06 ± 0.87	free
f	0.67 ± 0.12	0.55 ± 0.18	free
$c \times 10^{-3}$ $[\mathrm{MeV}/c^2]^{-1}$	-2.14 ± 0.19	-2.183 ± 0.059	free

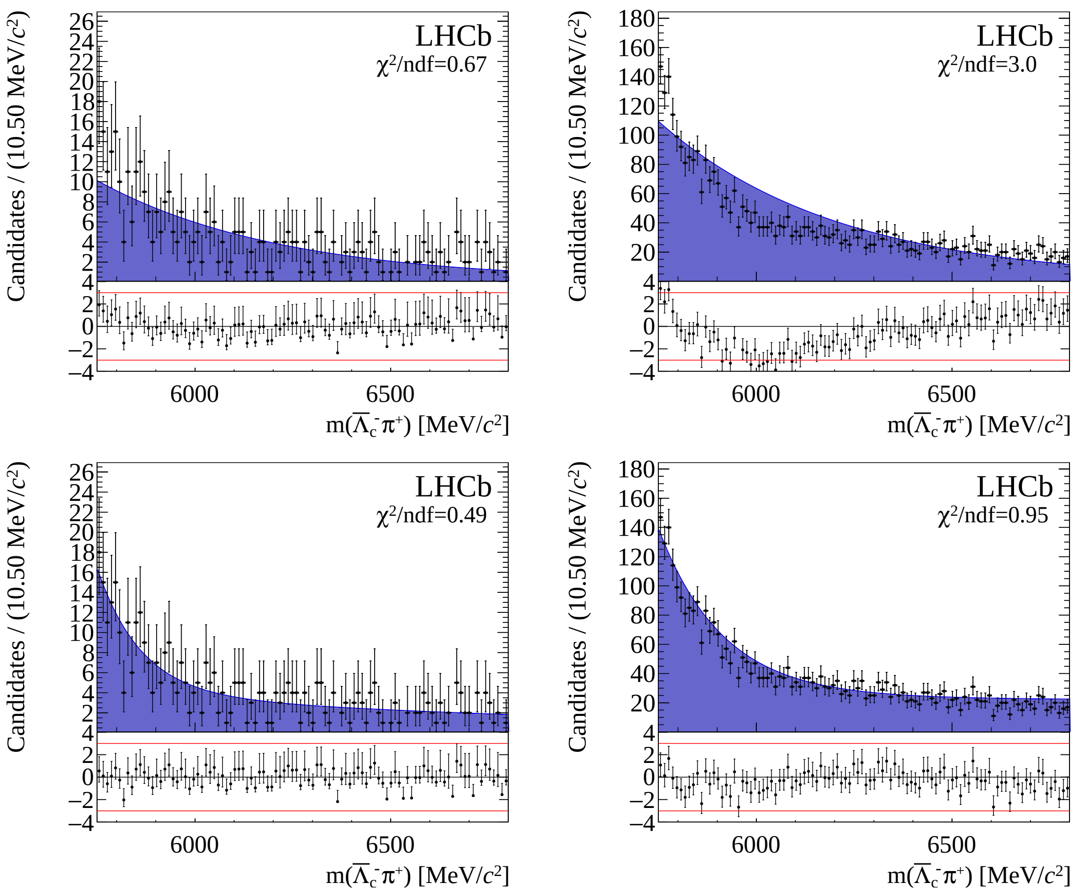

Figure 4.5: The invariant mass $m(\bar{\Lambda}_c^- \pi^+)$ distribution for the $\bar{\Lambda}_b^0$ sideband $m(\bar{\Lambda}_c^- \pi^+) \in [5750, 6800]\,\mathrm{MeV}/c^2$. In this region only the combinatorial background is considered. The results are split for the data taking period Run1 (left) and Run2 (right) as well as two parametrisations: a single exponential (top) and a double exponential (bottom). The lower part of each figure shows the residual of the data points with respect to the fit, normalised to the uncertainty of the data points.

For the analysis, the values of the yields of decays noted in Table 4.7: $n_{\overline{\Lambda}_b^0 \to \overline{\Lambda}_c^- \rho^+}$ and $n_{\overline{\Lambda}_b^0 \to \overline{\Sigma}_c^- \pi^+}$ are of importance, as the partially reconstructed backgrounds behaviour in correspondence to each other and the $\overline{\Lambda}_b^0 \to \overline{\Lambda}_c^- \pi^+$ decay channel is a great indicator whether the nominal mass fit is stable. The backgrounds enter the signal region $m(\overline{\Lambda}_c^- \pi^+) \in [m_{\overline{\Lambda}_b^0} - 50.00, m_{\overline{\Lambda}_b^0} + 50.00]\,\mathrm{MeV}/c^2$ for $\overline{\Lambda}_b^0$ baryon mass $m_{\overline{\Lambda}_b^0}$ ($\overline{\Lambda}_b^0$ and Λ_b^0 masses are equal and given by Table 3.4). The nominal mass fits for $\overline{\Lambda}_b^0 \to \overline{\Lambda}_c^- \pi^+$ Run1 and Run2 are shown in Fig. 4.6. Together with $\overline{\Lambda}_b^0 \to \overline{\Lambda}_c^- \pi^+$ yield, denoted $n_{\overline{\Lambda}_b^0 \to \overline{\Lambda}_c^- \pi^+}$, the parameters values after the nominal mass fit are listed in Table 4.9.

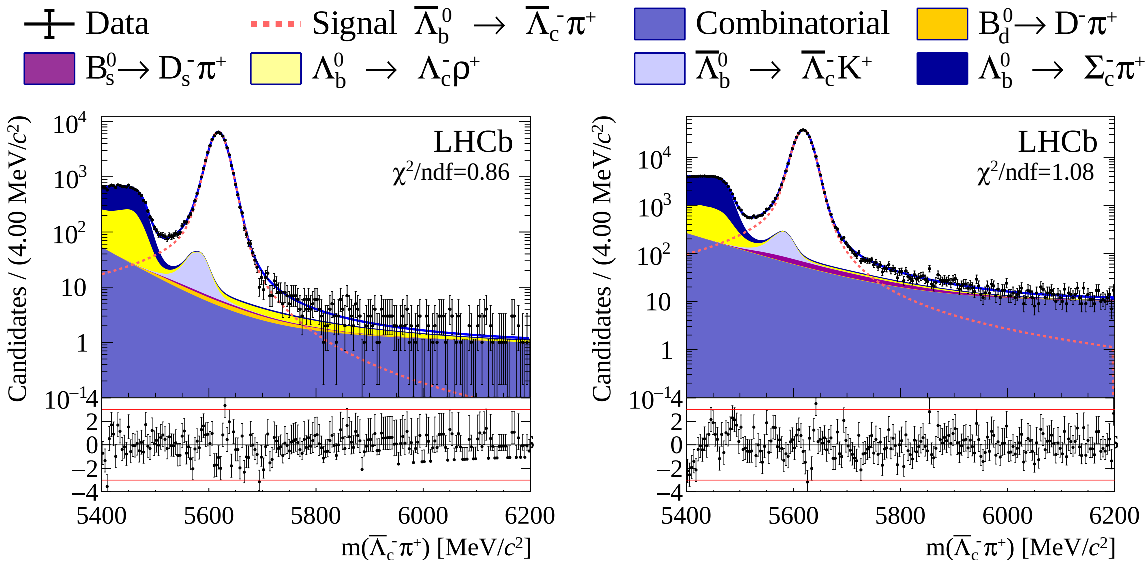

Figure 4.6: Nominal mass fit for $\overline{\Lambda}_b^0 \to \overline{\Lambda}_c^- \pi^+$ Run1 (left) and Run2 (right) in logarithmic scale with shared legend (top). The lower part of each figure shows the residual of the data points with respect to the fit, normalised to the uncertainty of the data points.

Table 4.9: Parameters describing the nominal invariant mass $m(\overline{\Lambda}_c^- \pi^+)$ fit in the $\overline{\Lambda}_b^0 \to \overline{\Lambda}_c^- \pi^+$ sample in range: $m(\overline{\Lambda}_c^- \pi^+) \in [5400, 6200]\,\mathrm{MeV}/c^2$. The signal range is defined $\pm 50\,\mathrm{MeV}/c^2$ around nominal $\overline{\Lambda}_b^0$ mass (see Table 3.4). The parameters $n_{\overline{\Lambda}_b^0 \to \overline{\Lambda}_c^- \rho^+}$ and $n_{\overline{\Lambda}_b^0 \to \overline{\Sigma}_c^- \pi^+}$ describe backgrounds yields, as given in Table 4.7, while $n_{\overline{\Lambda}_b^0 \to \overline{\Lambda}_c^- \pi^+}$ is the $\overline{\Lambda}_b^0 \to \overline{\Lambda}_c^- \pi^+$ yield. The corresponding results of the fit are shown in Fig. 4.6. Columns on the bottom describe the fit performance for $\overline{\Lambda}_b^0 \to \overline{\Lambda}_c^- \pi^+$ signal S and its total background B.

Parameter	Run1	Run2
$n_{\overline{\Lambda}_b^0 \to \overline{\Lambda}_c^- \pi^+}$	64050 ± 260	367820 ± 660
$n_{\overline{\Lambda}_b^0 \to \overline{\Lambda}_c^- \rho^+}$	4300 ± 1300	15700 ± 4400
$n_{\overline{\Lambda}_b^0 \to \overline{\Sigma}_c^- \pi^+}$	8000 ± 1400	60200 ± 3800

Period	S/B		$S/\sqrt{S+B}$	
	Signal range	Total range	Signal range	Total range
Run1	132.53	4.53	247.18	229.04
Run2	100.79	4.13	590.44	544.11

4.4. The invariant mass fit to the $\Lambda_b^0 \to D_s^- p$ sample

An invariant mass fit to the $\Lambda_b^0 \to D_s^- p$ sample under its own hypothesis is used in order to estimate the yield of $\Lambda_b^0 \to D_s^- p$ decay in the $\Lambda_b^0 \to D_s^- p$ data samples. The signal description follows the same functional form as for other decays. The numerical values of parameters are obtained from the dedicated fits to the simulation samples.

The specific background contributions to the fit are described in Tab. 4.10 together with how they contribute to the sample and in which data set can they be found. For the case of $\Lambda_b^0 \to D_s^- p$ decay, three different sources of background for $\Lambda_b^0 \to D_s^- p$ signal can be distinguished: the misidentified backgrounds ($B_s^0 \to D_s^- \pi^+$, $B_s^0 \to D_s^{\mp} K^{\pm}$, $B^0 \to D_s^- K^+$), the partially reconstructed backgrounds which occur due to missing particles in the final state ($\Lambda_b^0 \to D_s^{*-} p$) and the backgrounds that are both partially reconstructed and misidentified ($B_s^0 \to D_s^{*-} \pi^+$, $B_s^0 \to D_s^- \rho^+$ $B_s^0 \to D_s^{*-} \rho^+$, $B_s^0 \to D_s^{*\mp} K^{\pm}$, $B_s^0 \to D_s^{\mp} K^{*\pm}$, $B_s^0 \to D_s^{*\mp} K^{*\pm}$). Together with the signal $\Lambda_b^0 \to D_s^- p$, these yields constitute the subject of study.

Due to a low statistic of the $\Lambda_b^0 \to D_s^- p$ sample, the functional form of the combinatorial background parametrisation is taken as a single exponential without any further studies.

In order to stabilise fitting procedure some background components are merged in groups. Initial division includes three groups. The first group is the partially reconstructed background $\Lambda_b^0 \to D_s^{*-} p$, where no particles are misidentified. In the nominal mass fit, their yield is denoted $n_{\Lambda_b^0 \to D_s^{*-} p}$. The second group unites the partially reconstructed and misidentified $D_s^- \pi^+$-like backgrounds ($B_s^0 \to D_s^- \pi^+$, $B_s^0 \to D_s^{*-} \pi^+$, $B_s^0 \to D_s^- \rho^+$). For the purpose of these preliminary studies the contribution from the $B_s^0 \to D_s^{*-} \rho^+$ decays is neglected. These backgrounds can be merged into one compo-

Table 4.10: Specific backgrounds considered in the $\Lambda_b^0 \to D_s^- p$ sample.

Decay chain	How it contributes	Other sample
$B_s^0 \to D_s^- \pi^+$	$\pi^+ \to p$ (companion)	$B_s^0 \to D_s^- \pi^+$
$B_s^0 \to D_s^\mp K^\pm$	$K^+ \to p$ (companion)	$B_s^0 \to D_s^\mp K^\pm$
$B^0 \to D_s^- K^+$	$K^+ \to p$ (companion)	$B_s^0 \to D_s^\mp K^\pm$
$\Lambda_b^0 \to D_s^{*-} p \to D_s^- \gamma p$	Missing photon γ	N/A
$B_s^0 \to D_s^{*-} \pi^+ \to D_s^- \gamma \pi^+$	$\pi^+ \to p$ (companion), missing photon γ	$B_s^0 \to D_s^- \pi^+$
$B_s^0 \to D_s^- \rho^+ \to D_s^- \pi^+ \pi^0$	$\pi^+ \to p$ (companion), missing π^0	$B_s^0 \to D_s^- \pi^+$
$B_s^0 \to D_s^{*-} \rho^+ \to D_s^- \gamma \pi^+ \pi^0$	$\pi^+ \to p$ (companion), missing π^0 and γ	$B_s^0 \to D_s^- \pi^+$
$B_s^0 \to D_s^{*\mp} K^\pm \to D_s^\mp \gamma K^\pm$	$K^+ \to p$ (companion), missing photon γ	$B_s^0 \to D_s^\mp K^\pm$
$B_s^0 \to D_s^\mp K^{*\pm} \to D_s^\mp K^\pm \gamma$	$K^+ \to p$ (companion), missing photon γ	$B_s^0 \to D_s^\mp K^\pm$
$B_s^0 \to D_s^{*\mp} K^{*\pm} \to D_s^\mp \gamma K^\pm \gamma$	$K^+ \to p$ (companion), missing photons $\gamma\gamma$	$B_s^0 \to D_s^\mp K^\pm$

nent $B_s^0 \to D_s^{(*)-}(\pi^+, \rho^+)$ following the recursive procedure, similar to those performed for $B_s^0 \to D_s^- \pi^+$ and $B_s^0 \to D_s^\mp K^\pm$ samples (Sec. 4.1 and 4.2, Eq. (4.3) to (4.7)), just as the Eq. (4.8) shows for $n_{X \to Y}$ yields of $X \to Y$ decay and relative ratios denoted f_{1i} for $i+1$ decays merged:

$$\begin{aligned} n_{B_s^0 \to D_s^{(*)-}(\pi^+,\, \rho^+)} =& f_{11} \times n_{B_s^0 \to D_s^- \pi^+} \\ &+ (1 - f_{11}) \times f_{12} \times n_{B_s^0 \to D_s^{*-} \pi^+} \\ &+ (1 - f_{11}) \times (1 - f_{12}) \times n_{B_s^0 \to D_s^- \rho^+}. \end{aligned} \tag{4.8}$$

Similar recursive procedure is applied for the third group, for partially reconstructed and misidentified $D_s^\mp K^\pm$-like backgrounds ($B_s^0 \to D_s^\mp K^\pm$, $B_s^0 \to D_s^{*\mp} K^\pm$, $B_s^0 \to D_s^\mp K^{*\pm}$). To simplify the procedure, the preliminary model does not consider contributions from the $B_s^0 \to D_s^{*\mp} K^{*\pm}$ and $B^0 \to D_s^- K^+$, which are temporary neglected. These components will be added together with the constrains from the $B_s^0 \to D_s^\mp K^\pm$ fits to obtain the component $n_{B_{(s)}^0 \to D_s^{(*)\mp} K^{(*)\pm}}$ in Eq. (4.9) for relative ratios f_{2i} for $i+1$ decays merged:

$$\begin{aligned} n_{B_{(s)}^0 \to D_s^{(*)\mp} K^{(*)\pm}} =& f_{21} \times n_{B_s^0 \to D_s^\mp K^\pm} \\ &+ (1 - f_{21}) \times f_{22} \times n_{B_s^0 \to D_s^{*\mp} K^\pm} \\ &+ (1 - f_{21}) \times (1 - f_{22}) \times n_{B_s^0 \to D_s^\mp K^{*\pm}}. \end{aligned} \tag{4.9}$$

For the further simplification, two last groups, for partially reconstructed and misidentified $D_s^- \pi^+$-like and $D_s^\mp K^\pm$-like backgrounds can be merged into the group containing all the decays where the final state particle was misidentified as a proton p, thus the recursive procedure is applied once more to obtain the component $n_{B_{(s)}^0 \to D_s^{(*)\mp}(K^{(*)\pm},\, \pi^+,\, \rho^+)}$ using relative ratio f_{31}:

$$\begin{aligned} n_{B_{(s)}^0 \to D_s^{(*)\mp}(K^{(*)\pm},\, \pi^+,\, \rho^+)} =& f_{31} \times n_{B_{(s)}^0 \to D_s^{(*)\mp} K^{(*)\pm}} \\ &+ (1 - f_{31}) \times n_{B_s^0 \to D_s^{(*)-}(\pi^+,\, \rho^+)}. \end{aligned} \tag{4.10}$$

In the preliminary studies presented in this dissertation, the $D_s^-\pi^+$-like and $D_s^\mp K^\pm$-like ratios from the invariant mass fits (Sections 4.1 and 4.2) are used for constraints on the $\Lambda_b^0 \to D_s^- p$ fit. In the notation of Eq. (4.8), (4.9) and (4.10), these are the fractions of f_{11}, f_{12}, f_{21} and f_{22}, all set to constant values in the $\Lambda_b^0 \to D_s^- p$ nominal invariant mass fit.

The definitions between the fractions introduced in Sec. 4.1 and 4.2 slightly differ from the definitions for $\Lambda_b^0 \to D_s^- p$ backgrounds ratios (in Eq. (4.8)-(4.10)), e.g. Eq. (4.3) includes the $B_s^0 \to D_s^{*-}\rho^+$ channel, that was excluded from the Eq. (4.8), because of the expected negligible number of events in $\Lambda_b^0 \to D_s^- p$ background. Thus, the fractions obtained in Sec. 4.1 and 4.2 are recalculated for the case of $\Lambda_b^0 \to D_s^- p$ decay channel background consideration.

Moreover, the f_{31} fraction is set to constant values of 0.65 for Run1 and 0.68 for Run2, as obtained in the very preliminary estimations using the simulation and PID calibration samples. These preliminary studies suggest that in the $\Lambda_b^0 \to D_s^- p$ sample a kaon misdentification occurs about twice often then a pion misidentification.

In the analysis, the values of $n_{\Lambda_b^0 \to D_s^{*-} p}$ and $n_{B_{(s)}^0 \to D_s^{(*)\mp}(K^{(*)\pm},\, \pi^+,\, \rho^+)}$ are considered, as the partially reconstructed backgrounds behaviour in correspondence to the $\Lambda_b^0 \to D_s^- p$ decay channel gives an insight whether the nominal mass fit is stable. Together with $\Lambda_b^0 \to D_s^- p$ yield, denoted $n_{\Lambda_b^0 \to D_s^- p}$, these parameters values after the nominal mass fit are listed in Table 4.11. The nominal mass fit for $\Lambda_b^0 \to D_s^- p$ Run1 and Run2 is shown in Fig. 4.7. The signal region was $m(D_s^- p) \in [m_{\Lambda_b^0} - 50.00, m_{\Lambda_b^0} + 50.00]\,\mathrm{MeV}/c^2$, for Λ_b^0 baryon mass $m_{\Lambda_b^0}$ (given by Table 3.4).

The presented fits are preliminary estimations of the $\Lambda_b^0 \to D_s^- p$ signal yields, where the $\Lambda_b^0 \to D_s^- p$ process is seen with a significance larger than five standard deviations. The fractions obtained from the control samples stabilise the fitting procedure, but more improvements are possible. The absolute values of the $D_s^-\pi^+$-like and $D_s^\mp K^\pm$-like backgrounds can be estimated from the PID efficiency studies. In addition, due to lack of the dedicated simulation sample, the $B^0 \to D_s^- K^+$ contribution is temporary neglected. These can be a subject of future studies.

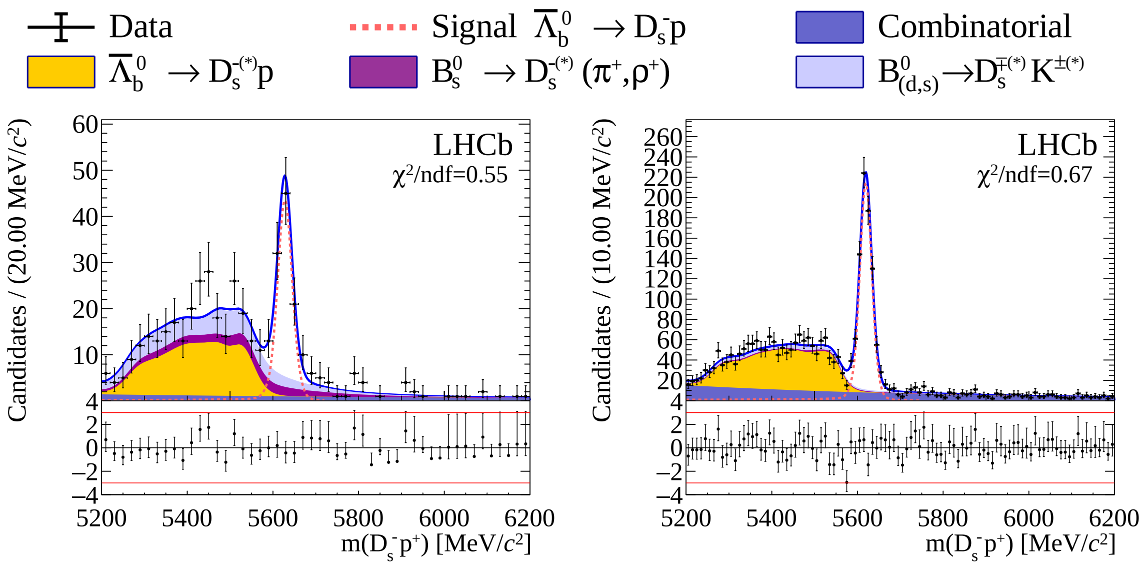

Figure 4.7: Nominal mass fit for $\Lambda_b^0 \to D_s^- p$ Run1 (left) and Run2 (right) with shared legend (top). The lower part of each figure shows the residual of the data points with respect to the fit, normalised to the uncertainty of the data points.

Table 4.11: Parameters describing the nominal invariant mass $m(D_s^- p)$ fit in the $\Lambda_b^0 \to D_s^- p$ sample in total range: $m(D_s^- p) \in [5200, 6200]\,\text{MeV}/c^2$. The signal range is defined $\pm 50\,\text{MeV}/c^2$ around nominal Λ_b^0 mass (see Table 3.4). The parameters $n_{\Lambda_b^0 \to D_s^{*-} p}$ and $n_{B_{(s)}^0 \to D_s^{(*)\mp}(K^{(*)\pm},\, \pi^+,\, \rho^+)}$ describe backgrounds yields, as given by Eq. (4.8)-(4.10), while $n_{\Lambda_b^0 \to D_s^- p}$ is the $\Lambda_b^0 \to D_s^- p$ yield. The corresponding results of the fit are shown in Fig. 4.7. Columns on the bottom describe the fit performance for $\Lambda_b^0 \to D_s^- p$ signal S and its total background B.

Parameter	Run1	Run2
$n_{\Lambda_b^0 \to D_s^- p}$	102 ± 14	835 ± 35
$n_{\Lambda_b^0 \to D_s^{*-} p}$	155 ± 37	1080 ± 100
$n_{B_{(s)}^0 \to D_s^{(*)\mp}(K^{(*)\pm},\, \pi^+,\, \rho^+)}$	141 ± 66	170 ± 210

Period	S/B		$S/\sqrt{S+B}$	
	Signal range	Total range	Signal range	Total range
Run1	3.03	0.30	8.44	4.84
Run2	6.13	0.41	25.90	15.59

Chapter 5

Results

For this thesis, the estimation of yields of $\Lambda_b^0 \to D_s^- p$ and $\overline{\Lambda}_b^0 \to \overline{\Lambda}_c^- \pi^+$ was presented. In order to obtain unbiased signal and background contributions, a data-driven method is proposed. Two control modes, the $B_s^0 \to D_s^- \pi^+$ and $B_s^0 \to D_s^\mp K^\pm$ decays, are used. The functional form of the combinatorial background parametrisation is verified by the dedicated study of the beauty hadron invariant mass sideband. The thesis presents the preliminary fits to the four decays of interest: $B_s^0 \to D_s^\mp K^\pm$, $B_s^0 \to D_s^- \pi^+$, $\overline{\Lambda}_b^0 \to \overline{\Lambda}_c^- \pi^+$ and $\Lambda_b^0 \to D_s^- p$ with description of their signal and background composition. The mutual relations among them can be employed in order to stabilise fitting procedure in lower statistic samples. Demonstrated procedure is expected to be a foundation for the future determination of $\Lambda_b^0 \to D_s^- p$ and $\overline{\Lambda}_b^0 \to \overline{\Lambda}_c^- \pi^+$ branching fractions ratio for the very first time, as given by Eq. (1.3). The values of crucial yields that were obtained in this analysis are described in Table 5.1.

Table 5.1: Yields of the nominal invariant mass fits for the channels of $\Lambda_b^0 \to D_s^- p$ samples analysis. Total ranges of $m(D_s^- \pi^+), m(D_s^\mp K^\pm)$ are equal to $[5000, 6000]\,\mathrm{MeV}/c^2$ and for $m(\overline{\Lambda}_c^- \pi^+), m(D_s^- p)$ to $[5400, 6200]\,\mathrm{MeV}/c^2$. The signal range for $m(D_s^- \pi^+), m(D_s^\mp K^\pm)$ is $[5316.89, 5416.89]\,\mathrm{MeV}/c^2$ and for $m(\overline{\Lambda}_c^- \pi^+), m(D_s^- p)$ it is $[5569.58, 5669.58]\,\mathrm{MeV}/c^2$. Complete results of the invariant mass fits are written in Tables 4.3, 4.6, 4.9 and 4.11 for $B_s^0 \to D_s^- \pi^+$, $B_s^0 \to D_s^\mp K^\pm$, $\overline{\Lambda}_b^0 \to \overline{\Lambda}_c^- \pi^+$ and $\Lambda_b^0 \to D_s^- p$ decays.

Decay	Run1	Run2
$\Lambda_b^0 \to D_s^- p$	102 ± 14	835 ± 35
$\overline{\Lambda}_b^0 \to \overline{\Lambda}_c^- \pi^+$	64050 ± 260	367820 ± 660
$B_s^0 \to D_s^- \pi^+$	39040 ± 210	184100 ± 420
$B_s^0 \to D_s^\mp K^\pm$	2064 ± 49	10450 ± 110

The next step for the analysis would be to include the $B_s^0 \to D_s^- \pi^+$- and $B_s^0 \to D_s^\mp K^\pm$-like backgrounds estimates from $B_s^0 \to D_s^- \pi^+$ and $B_s^0 \to D_s^\mp K^\pm$ samples in the analysis of $\Lambda_b^0 \to D_s^- p$ invariant mass spectra, just as described in Sec. 3.1. Moreover, including the selection efficiencies for all consecutive cuts applied on considered samples would be a natural addition to the clean analysis description. However, the dedicated calibration samples have to be used to obtain precise values for efficiency calculations [51] and for the sake of the thesis this step was omitted.

Appendix A

Definitions

The selection of $\Lambda_b \to D_s p$ decay over the background is a highly challenging task. To distinguish the signal, a procedure involving many variables was convoluted. This Appendix is meant to sum up all the most important definitions in a clean manner. Among the parameters and concepts used in the parameters a few can be mentioned [57]:

- primary vertex (PV): the position of the proton-proton collision;
- secondary vertex (SV): the position of the decay of long-lived particles;
- mother particle: the particle from which another particle comes, e.g. B_s is a mother particle for a D_s meson in a $B_s \to D_s K$ decay;
- daughter particle: complementary to the previous definition: a particle created out from a decay of a certain other particle;
- impact parameter (IP): the minimal distance, in perpendicular direction, between the primary vertex and the reconstructed track. For the LHCb experiment, the χ^2 impact parameter in often used, calculated as $\mathrm{IP}\chi^2 \propto \frac{\mathrm{IP}^2}{\sigma_{\mathrm{IP}}^2}$ for σ_{IP} the uncertainty of the impact parameter;
- semileptonic decay: a decay caused by the weak force, in which a lepton (with a corresponding neutrino) is produced in addition to one or more hadrons. The semileptonic cut gets rid of decays where one of the final state particle is a lepton;
- flight distance (FD): the distance between the primary and secondary vertex (mother and daughter particle vertices);
- BDT: Boosted Decision Tree, an improved machine learning algorithm of decision tree (the concept of a decision tree is not to reject right away events that fail a criterion, and instead to check whether other criteria may help to classify these events properly) for distinguishing signal and background via variables being the linear combination of physical observables. A BDT variable is used to quantify the probability of an event belonging to the signal or the background. More in [48].

Appendix B

Tables of selection cuts

Table B.1: Kinematic selection.

Description	Requirement
Applied for all decays:	
Pseudorapidity η	$\in$ [2,5]
RICH information	$== 1$
Number of tracks	$\in$ [15,500]
Companion p	$\in$ [10, 150] GeV/c
Companion p_T	$\in$ [1.0, 45] GeV/c
Kaon and pion momentum p	$\in$ [2, 150] GeV/c
Proton momentum	$\in$ [10, 150] GeV/c
Kaon, pion transverse momentum p_T	$\in$ [0.25, 45] GeV/c
Charm meson flight distance (FD)	> 0
Charm meson FD χ^2	> 2
Charm candidate lifetime:	> 0
B_s invariant mass: $m(B_s^0)$	$\in$ [5000, 7000] MeV/c^2
BDT response	> 0.4
Specific cuts for $B_s^0 \to D_s^- h^+$ (h is a hadron) and $\Lambda_b \to D_s p$:	
Charm invariant mass: $m(D_s^-)$	$\in$ [1950, 1990] MeV/c^2
Λ_b invariant mass: $m(\Lambda_b^0)$	$\in$ [5000, 7000] MeV/c^2
Specific cuts for $\Lambda_b \to \Lambda_c \pi$:	
Semileptonic cut	$== 0$
Charm invariant mass: $m(\Lambda_c^+)$	$\in$ [2270, 2302] MeV/c^2
Λ_b invariant mass: $m(\Lambda_b^0)$	$\in$ [5400, 6000] MeV/c^2

Table B.2: PID selection (applied for $B_s^0 \to D_s^- h^+$ (h is a hadron), $\Lambda_b \to D_s p$ and $\Lambda_b \to \Lambda_c \pi$).

Description	Requirement
D_s children:	
PIDK of both kaons	> 5
PIDK of pion	< 0
Λ_c children:	
ProbNNp of proton	> 0.6
PIDK of kaon	> 0
PIDK of pion	< 5
Companion PIDK for:	
$B_s \to D_s \pi$ and $\Lambda_b \to \Lambda_c \pi$	< 0
$B_s \to D_s K$	> 10
Companion ProbNNp for $\Lambda_b \to D_s p$:	
Run1	> 0.7
Run2	> 0.9

Table B.3: Specific background vetoes (for $B_s^0 \to D_s^- h^+$, where h is a hadron, and $\Lambda_b \to D_s p$).

Description	Requirement
D^0 veto:	
$m(K^+K^-)$	$< 1800\,\mathrm{MeV}/c^2$
D^- veto either:	
PIDK of same charge K	> 10, or
$m(D_s^-)$ under D^- hypothesis	$\notin [1840,\, 1900]\,\mathrm{MeV}/c^2$
Λ_c veto either:	
same charge K PIDK-PIDp	> 5, or
$m(D_s^-)$ under Λ_c hypothesis	$\notin [2255,\, 2315]\,\mathrm{MeV}/c^2$
Λ_c veto:	
PIDp	< 10
J/ψ veto:	
Semileptonic cut	$== 0$

Bibliography

[1] Herwig Schopper, *Particle Physics Reference Library. Volume 1: Theory and Experiments*, Springer, p. 1-5, 2020.

[2] Isaac Newton, *Optics*, Query 31, London 1718.

[3] C. D. Anderson, *The positive electron*, Phys. Rev. **43** (1933) 491.

[4] W. Pauli, *Pauli letter collection: letter to Lise Meitner*, Typed copy.

[5] Immanuel Kant, *Kritik der reinen Vernunft*, see, e.g., Meiner Verlag, Hamburg 1998, or translation by N.K. Smith, London, MacMillan 1929, 1781.

[6] Emmy Noether, *Nachr. d. königl. Gesellschaft d. Wissenschaften zu Göttingen*, p. 235, 1918.

[7] C. S. Wu *et al.*, *Experimental test of parity conservation in beta decay*, Phys. Rev. **105** (1957) 1413.

[8] T. D. Lee and C. N. Yang, *Question of parity conservation in weak interactions*, Phys. Rev. **104** (1956) 254.

[9] Carsten Burgard, *Example: Standard model of physics*, `https://texample.net/tikz/examples/model-physics/`. Accessed: 2021-05-04.

[10] N. Cabibbo, *Unitary Symmetry and Leptonic Decays*, Phys. Rev. Lett. **10** (1963) 531.

[11] M. Kobayashi and T. Maskawa, *CP Violation in the Renormalizable Theory of Weak Interaction*, Prog. Theor. Phys. **49** (1973) 652.

[12] M. Bargiotti *et al.*, *Present knowledge of the Cabibbo-Kobayashi-Maskawa matrix*, Rivista del Nuovo Cimento **23** (2000) 4.

[13] A. D. Sakharov, *Violation of CP invariance, C asymmetry, and baryon asymmetry of the universe*, Soviet Physics Uspekhi **34** (1991) 392.

[14] D. H. Perkins, *The Sakharov criteria* in *Introduction to high energy physics*, The Press Syndicate of The University of Cambridge, 2000.

[15] The CKMfitter group webpage, `http://ckmfitter.in2p3.fr/`. Accessed: 2021-05-24.

[16] D. Abbaneo *et al.*, *The CKM matrix and the Unitarity Triangle. Workshop, CERN, Geneva, Switzerland, 13-16 Feb 2002: Proceedings*, `arXiv:hep-ph/0304132arXiv:hep-ph/0304132`, pp. 3–6.

[17] The global CKM fit in the large (ρ-bar, η-bar) plane: Constraints in the (ρ-bar, η-bar) plane. The red hashed region of the global combination corresponds to 68% CL., `http://ckmfitter.in2p3.fr/www/results/plots_summer19/ckm_res_summer19.html`. Accessed: 2021-05-04.

[18] M. Fiore, *New results on semileptonic b decays from LHCb*, in *Meeting of the APS Division of Particles and Fields*, 2015, `arXiv:1511.00105`.

[19] J. P. Lees *et al.*, *Study of $\bar{B} \to X_u \ell \nu^-$ decays in $B\bar{B}$ events tagged by a fully reconstructed B-meson decay and determination of $|V_{ub}|$*, Physical Review D **86** (2012) .

[20] Particle Data Group, P. A. Zyla *et al.*, *Review of particle physics: Semileptonic b-Hadron Decays, Determination of V_{cb}, V_{ub}*, Prog. Theor. Exp. Phys. **2020** (2020) 083C01.

[21] LHCb collaboration, R. Aaij *et al.*, *Measurement of CP asymmetry in $B_s^0 \to D_s^{\mp} K^{\pm}$ decays*, JHEP **03** (2018) 059, `arXiv:1712.07428`.

[22] L. Evans and P. Bryant, *LHC machine*, Journal of Instrumentation **3** (2008) S08001.

[23] A. Hoecker, *Physics at the LHC Run-2 and Beyond*, in *2016 European School of High-Energy Physics*, 2016, `arXiv:1611.07864`.

[24] ATLAS, G. Aad *et al.*, *The ATLAS Experiment at the CERN Large Hadron Collider*, JINST **3** (2008) S08003.

[25] CMS, S. Chatrchyan *et al.*, *The CMS Experiment at the CERN LHC*, JINST **3** (2008) S08004.

[26] T. A. Collaboration *et al.*, *The ALICE experiment at the CERN LHC*, Journal of Instrumentation **3** (2008) S08002.

[27] LHCb, A. A. Alves, Jr. *et al.*, *The LHCb Detector at the LHC*, JINST **3** (2008) S08005.

[28] Quench Simulation of Superconducting Magnets with Commercial Multi-physics Software, Figure 2, The Large Hadron Collider, Scientific Figure on ResearchGate. `https://www.researchgate.net/figure/The-Large-Hadron-Collider-5_fig2_283213754`. Accessed 8 May, 2021.

[29] Harp, *LHCb detector view among the bending plane*, `https://commons.wikimedia.org/wiki/File:Lhcbview.jpg`. Public Domain, Accessed: 2021-05-10.

[30] S. W. Maddrell-Mander, *An Angular Analysis of $B^+ \to K^+e^+e^-$ Decays at the LHCb Experiment*, 2020. Presented 25 Feb 2021. https://cds.cern.ch/record/2761005.

[31] LHCb Collaboration, R. Antunes-Nobrega *et al.*, *LHCb reoptimized detector design and performance: Technical Design Report*, Technical design report. LHCb, CERN, Geneva, 2003. http://cds.cern.ch/record/630827.

[32] J. Gassner, M. Needham, and O. Steinkamp, *Layout and Expected Performance of the LHCb TT Station*, CERN, Geneva, LHCb-2003-140, 2004. http://cds.cern.ch/record/728548.

[33] LHCb Collaboration, P. R. Barbosa-Marinho *et al.*, *LHCb inner tracker: Technical Design Report*, Technical design report. LHCb, CERN, Geneva, 2002. Revised version number 1 submitted on 2002-11-13 14:14:34. http://cds.cern.ch/record/582793.

[34] R. Arink *et al.*, *Performance of the LHCb outer tracker*, Journal of Instrumentation **9** (2014) P01002.

[35] LHCb Collaboration, *LHCb detector performance*, International Journal of Modern Physics A **30** (2015) 1530022.

[36] R. Aaij *et al.*, *Selection and processing of calibration samples to measure the particle identification performance of the LHCb experiment in Run 2*, Eur. Phys. J. Tech. Instr. **6** (2018) 1, arXiv:1803.00824.

[37] M. Tervoert, *First observation of the decay $\Lambda_b^0 \to D_s^p$*, 2018. Presented 2018.

[38] Particle Data Group, P. A. Zyla *et al.*, *Review of particle physics*, Prog. Theor. Exp. Phys. **2020** (2020) 083C01.

[39] LHCb collaboration, *Updated average f_s/f_d b-hadron production fraction ratio for 7 TeV pp collisions*, LHCb-CONF-2013-011, 2013.

[40] LHCb collaboration, R. Aaij *et al.*, *Measurement of the $\Lambda_b^0 \to J/\psi\Lambda$ angular distribution and the Λ polarisation in pp collisions*, JHEP **06** (2020) 110, arXiv:2004.10563.

[41] A. Puig, *The LHCb trigger in 2011 and 2012*, CERN, Geneva, LHCb-PUB-2014-046, CERN-LHCb-PUB-2014-046, 2014. http://cds.cern.ch/record/1970930.

[42] A. Satta, *The LHCb L0 trigger and related detectors*, Eur. Phys. J. C **34** (2004) S411.

[43] R. Aaij *et al.*, *The LHCb trigger and its performance in 2011*, Journal of Instrumentation **8** (2013) P04022.

[44] LHCb, R. Aaij *et al.*, *Design and performance of the LHCb trigger and full real-time reconstruction in Run 2 of the LHC*, JINST **14** (2019) P04013, arXiv:1812.10790.

[45] W. D. Hulsbergen, *Decay chain fitting with a Kalman filter*, Nucl. Instrum. Meth. **A552** (2005) 566, arXiv:physics/0503191.

[46] A. Powell, *Particle Identification at LHCb. Particle ID in LHCb*, 2011. https://cds.cern.ch/record/1322666.

[47] R. Aaij *et al.*, *Selection and processing of calibration samples to measure the particle identification performance of the LHCb experiment in Run 2*, EPJ Tech. Instrum. **6** (2019) 1, arXiv:1803.00824.

[48] Y. Coadou, *Boosted Decision Trees and Applications*, EPJ Web of Conferences **55** (2013) 02004.

[49] LHCb collaboration, R. Aaij *et al.*, *Measurement of the branching fraction of the $B^0 \to D_s^+\pi^-$ decay*, Eur. Phys. J. **C81** (2021) 314, arXiv:2010.11986.

[50] LHCb collaboration, R. Aaij *et al.*, *Precise determination of the B_s^0–$\bar{B}_s^0$ oscillation frequency*, arXiv:2104.04421, Submitted to Nature Physics.

[51] L. Anderlini *et al.*, *The PIDCalib package*, CERN, Geneva, LHCb-PUB-2016-021, CERN-LHCb-PUB-2016-021, 2016. https://cds.cern.ch/record/2202412.

[52] K. Cranmer, *Kernel Estimation in High Energy Physics.*, Comput. Phys. Commun. **136** (2001), pp. 198–207 https://doi.org/10.1016/S0010-4655(00)00243-5.

[53] R. Brun and F. Rademakers, *ROOT: An object oriented data analysis framework*, Nucl. Instrum. Meth. **A389** (1997) p. 81.

[54] LHCb, R. Aaij *et al.*, *Measurements of the branching fractions of the decays $B_s^0 \to D_s^\mp K^\pm$ and $B_s^0 \to D_s^-\pi^+$*, JHEP **06** (2012) p. 115, arXiv:1204.1237.

[55] LHCb, R. Aaij *et al.*, *Measurement of CP asymmetry in $B_s^0 \to D_s^\mp K^\pm$ decays*, JHEP **03** (2018) p. 059, arXiv:1712.07428.

[56] LHCb, R. Aaij *et al.*, *Study of the kinematic dependencies of Λ_b^0 production in pp collisions and a measurement of the $\Lambda_b^0 \to \Lambda_c^+\,\pi^-$ branching fraction*, JHEP **08** (2014) p. 143, arXiv:1405.6842.

[57] A. Dziurda, *Studies of time-dependent CP violation in charm decays of B_s^0 mesons*, PhD thesis, Cracow, INP, 2015, https://cds.cern.ch/record/2115353.